Tectonophysics 898 (2025) 230628

Contents lists available at ScienceDirect

Tectonophysics

journal homepage: www.elsevier.com/locate/tecto

Reactivation of critically-stressed basement faults and related induced seismicity in the southeastern Sichuan basin

Mengke An [a,b], Rui Huang [b,c], Derek Elsworth [b,d], Fengshou Zhang [c,*], Zhen-Yu Yin [a,*], Liuke Huang [e], Zhengyu Xu [f]

[a] Department of Civil and Environmental Engineering, The Hong Kong Polytechnic University, Hung Hom, Kowloon, Hong Kong 100872, China
[b] Department of Energy and Mineral Engineering, EMS Energy Institute and G3 Center, The Pennsylvania State University, University Park, PA 16802, USA
[c] Department of Geotechnical Engineering, College of Civil Engineering, Tongji University, Shanghai 200092, China
[d] Department of Geosciences, The Pennsylvania State University, University Park, PA 16802, USA
[e] School of Civil Engineering and Architecture, Southwest Petroleum University, Chengdu, Sichuan 610500, China
[f] PetroChina Hangzhou Institute of Geology, Hangzhou, China

ARTICLE INFO

Keywords:
Basement fault stability
Geo-energy extraction/storage
Fault reactivation
Gouge mineralogy
Poroelastic stress transfer
Fault aseismic slips

ABSTRACT

The southeastern Sichuan basin possesses abundant gas shale resources that are currently being recovered. The basement strata are seismically active making it important to understand the effect of fluid injection during geo-energy extraction and storage. We recovered outcropping basement rocks and conducted friction experiments on simulated rock gouge to assess the potential for frictional stability. Meanwhile, we also calculated the poroelastic Coulomb stresses resulting from fluid injection to define the impact of stress perturbations on fault stability. These results are combined with the seismic reflection images to analyze the seismic potential. Results indicate the basement rocks include clay-lean granites and sandstones and clay-rich slates; gouge frictional strength and stability are controlled by the clay contents. The gouge frictional strength monotonically decreases and fault stability is enhanced with increasing clay content. Poroelastic stresses induced by fluid injection can reactivate critically-stressed faults within 2 km of the injection site, but decay rapidly with increasing distance. The experimental-modelling results combined with seismic reflection profiles indicate that basement fault stability is controlled by various factors, including fault aseismic slip in the pressurized zones, poroelastic stress transfer from fluid injection and gouge mineralogy. These results have important implications for understanding instability of basement faults induced by fluid injection during energy extraction and storage and contribute to reducing seismic hazard in the southeastern Sichuan basin.

1. Introduction

The Sichuan basin of southwest China (Fig. 1a) is rich in shale oil/gas and mineable salt deposits and is also a promising area for carbon storage (CCS) in the subsurface, especially in the southeast (Lei et al., 2019; Ma and Xie, 2018; Sun et al., 2020; Zhang et al., 2022). Such activities typically involve fluid injection (Rubinstein and Mahani, 2015; Sun et al., 2017). One potential carbon storage method is the pumping the captured and compressed carbon dioxide (CO_2) into depleted oil and gas reservoirs or saline aquifers (Bickle, 2009). Consequently, both deep energy recovery and storage may result in the reactivation of deep faults and related seismicity (Ellsworth, 2013; Elsworth et al., 2016; Ge and Saar, 2022; Moein et al., 2023).

We use the shale gas projects in the Changning-Weiyuan-Luzhou national shale gas demonstration blocks of the southeastern Sichuan Basin as an example (Fig. 1a). The number of earthquakes from January 2009 to June 2022 in these three blocks are shown in Fig. 1b. Horizontal well drilling for hydraulic fracturing in southeastern Sichuan Basin was initiated in 2011, while the systematic hydraulic fracturing for shale gas recovery began in 2014 (Lei et al., 2017). Before 2011, the number of earthquakes in each half year were typically <500. However, a sharp increase in frequency was observed since 2014 where the semi-annual frequency was >8500, indicating a strong correlation between fluid injection and the observed clusters of earthquakes. Current examinations have included evaluation of overpressures, Coulomb failure stresses (An et al., 2021; Lei et al., 2017, 2019), microseismic

* Corresponding authors.
E-mail addresses: fengshou.zhang@tongji.edu.cn (F. Zhang), zhenyu.yin@polyu.edu.hk (Z.-Y. Yin).

https://doi.org/10.1016/j.tecto.2025.230628
Received 5 September 2024; Received in revised form 18 November 2024; Accepted 17 January 2025
Available online 21 January 2025

monitoring and analysis (Chen et al., 2018; Meng et al., 2019; Yang et al., 2021; Zhang et al., 2019a), the frictional properties of shale reservoir rock faults (An et al., 2020a, 2020b; Fang et al., 2018), casing deformation (Chen et al., 2017; Xi et al., 2018), earthquake focal mechanisms (Liu and Zahradník, 2020), tomographic observations (Tan et al., 2023) and subsurface velocity structure (Li et al., 2023). However, most of these studies have focused on earthquakes in the reservoirs and neglect the impacts of fault stability in basement rocks (Fig. 1c). Understanding fault stability and destructive earthquakes that nucleate in the basement are important to understand (Liu et al., 2021; Su et al., 2023).

Currently, there are three widely accepted models that interpret mechanisms of injection-induced earthquakes (Fig. S1, supporting information). The first model attributes fault instability to direct fluid pressure diffusion, contributing to increased pore fluid pressures and reduced effective stresses along the fault. This model requires a highly permeable pathway between the reservoir and the deep faults (Bao and Eaton, 2016; Azad et al., 2017; Raleigh et al., 1976). In the second model, fault reactivation is induced by solid stress changes driven by poro-thermalelastic stressing of the rock matrix, with fault loading applied without direct hydrologic connection (Segall and Lu, 2015; Deng et al., 2016). In the third model, unstable sliding may result from pore pressure-driven aseismic slip in the fluid diffusion region. Meanwhile, this model also requires a permeable channel between the reservoir and the deep fault (Bhattacharya and Viesca, 2019; Garagash and Germanovich, 2012; Eyre et al., 2019).

The basement rocks in the southeastern Sichuan Basin are primarily within the Proterozoic Kangding (i.e., Ebian) Group, Banxi Group and Granite, with the basement rocks in the Changning and Luzhou blocks located in the Banxi Group and the basement rocks of the Weiyuan block located in the Ebian Group and Granite (Fig. 2a). According to the exploration well data (He et al., 2019; Xu et al., 2019), the thickness of the sedimentary strata from the Quaternary to the Sinian in the southeastern Sichuan Basin spans 6–10 km in depth with most geoengineering activities conducted at depths of 2–4 km (Fig. 2b). The rocks in the Banxi Group are dominated by slates, while the Ebian Group

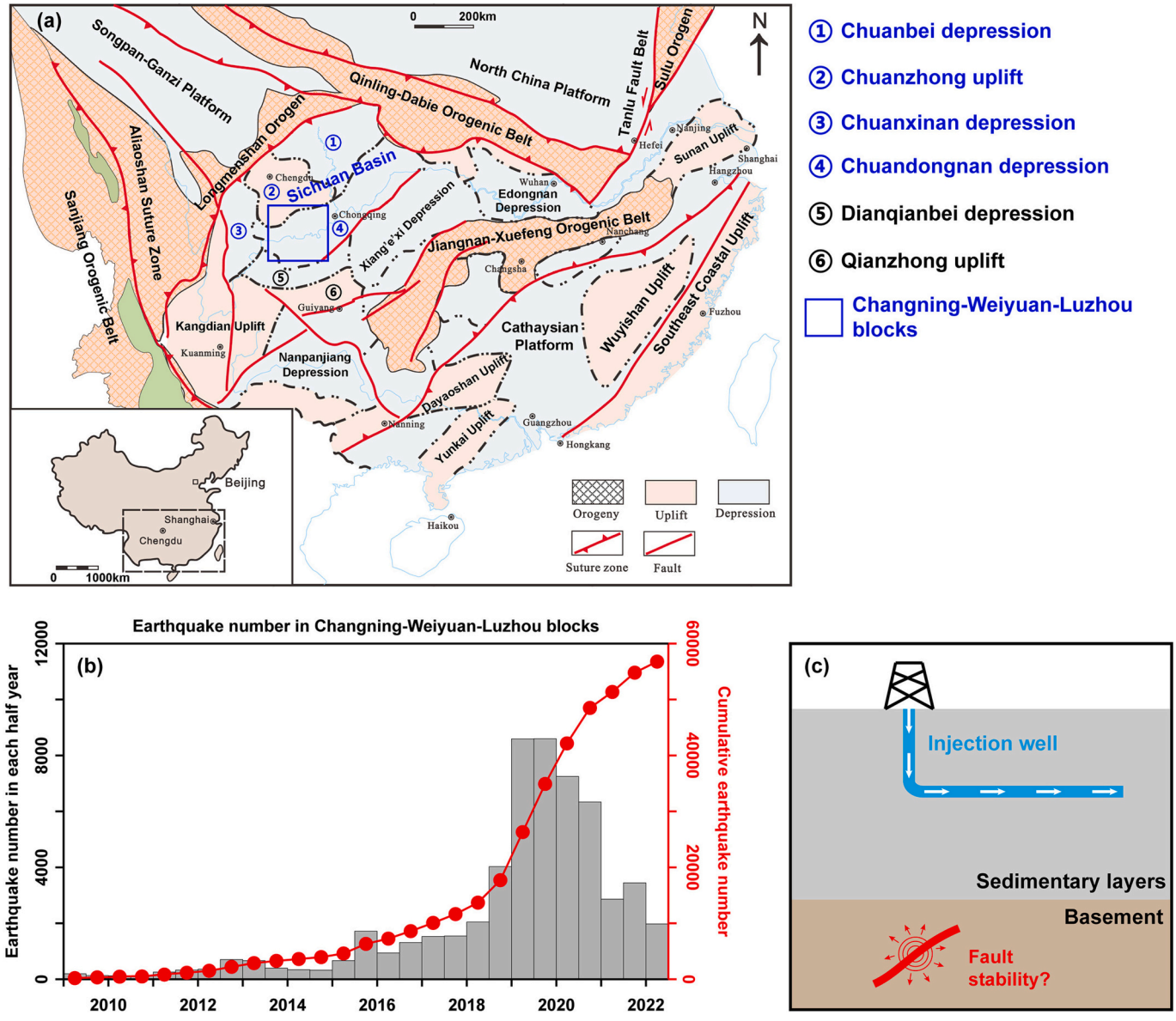

Fig. 1. (a) Tectonic map showing the locations in the Sichuan Basin of the Changning-Weiyuan-Luzhou blocks of southern China. Figure revised from Xu et al. (2019). (b) Number of earthquakes with magnitudes $M_L \geq 0$ from January 2009 to June 2022 in the Changning-Weiyuan-Luzhou blocks, including the number of earthquakes in each half year and the cumulative number of earthquakes. The earthquake data are derived from https://data.earthquake.cn. (c) A schematic showing the basement fault stability in response to fluid injection in the upper sedimentary layers.

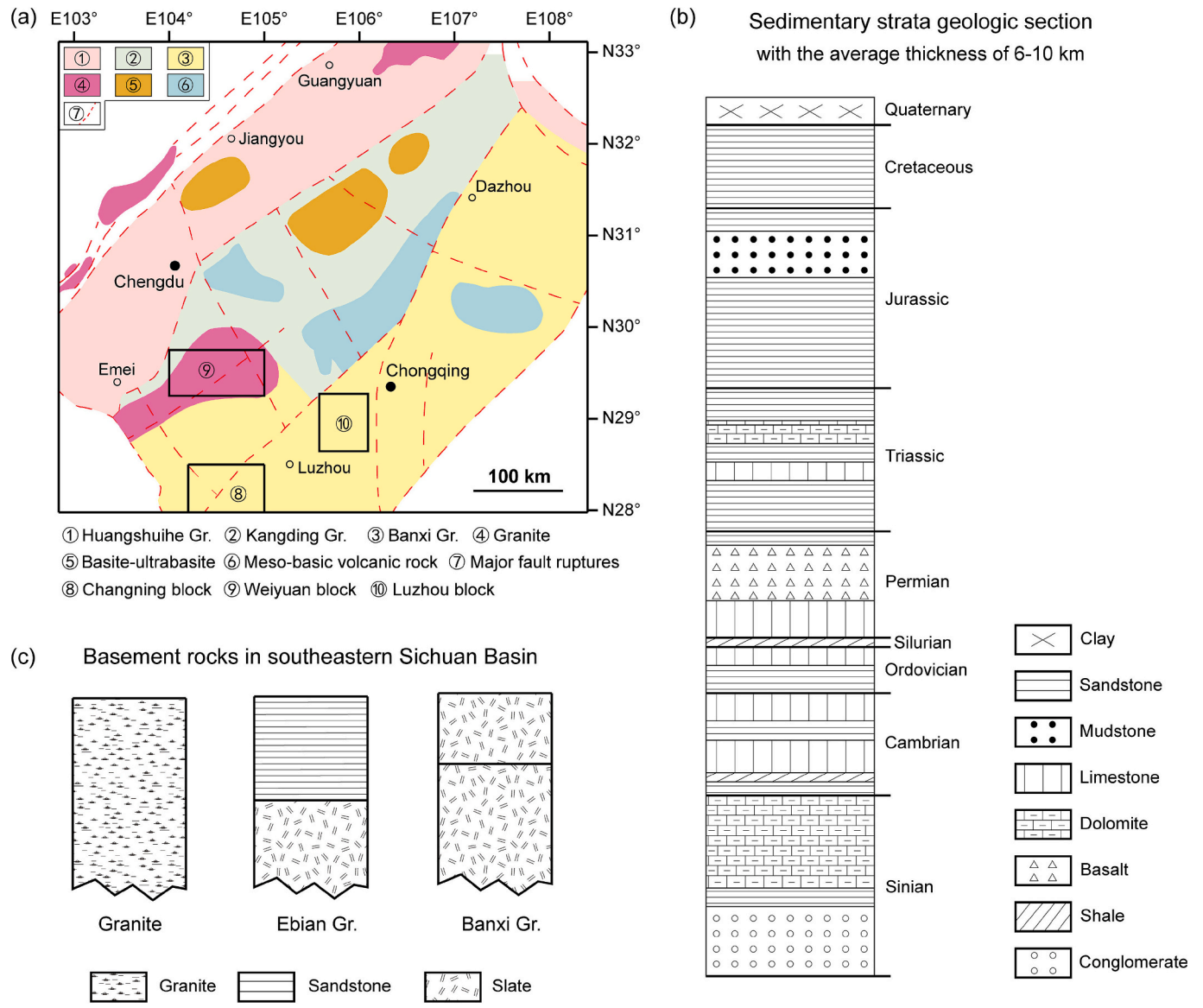

Fig. 2. (a) Distributions of the basement rocks in the Changning-Weiyuan-Luzhou blocks in Sichuan Basin. (b) Sedimentary strata geologic section with an average thickness of 6–10 km. The geologic section data were derived from the Weiyuan block. (c) Basement rocks in southeastern Sichuan Basin, including the Lower Proterozoic Granite, Ebian Group (Gr.) and Banxi Group rocks. The legends in (b) and (c) show the rock lithology.

rocks primarily include sandstones and slates (Fig. 2c). We explore models of fault reactivation and the spawning of earthquakes. We postulate that three enabling requirements are associated with basement fault stability. Firstly, the basement should have seismogenic zones with potentially unstable faults in the basement. Secondly, based on the first and third models, the basement faults could be reactivated by permeable channels from the reservoir to the basement or large thrust faults extending from the reservoir to the basement. Thirdly, based on the second model, the poroelastic stress perturbations could reactivate critically-stressed faults in the basement.

Based on this background, we recovered Proterozoic Granite and Ebian Group block samples from outcrops in the city of Leshan in Sichuan province, and Banxi Group rocks from outcrops in the cities of Guiyang & Zunyi in Guizhou province. Details of these basement rocks are shown in Figs. 3 and 4. The rocks in the upper Ebian Group are primarily metasandstone, while the argillaceous and gray-green slates dominate the middle Ebian Group (Fig. 3). Both the sandy and argillaceous slates are observed in the Banxi Group (Fig. 4). These rocks were deposited in the same geologic period as the deep basement rocks but exposed in the outcrops by multi-stage tectonic movements, and thus these rocks are likely representative of the deep basement rocks. We use these properties to explore potential seismogenic zones by applying rate-and-state friction (RSF) theory. Then, we use poroelastic stress perturbations from fluid injection and induced changes in Coulomb failure stress to define controls of poroelastic effects on fault stability. Finally, we use experimental and modelling results combined with the seismic reflection profile to analyze the seismic potential.

2. Experimental and modelling methods

2.1. Experiment materials

The X-ray diffraction (XRD) technique was employed to determine the mineral proportions of eleven samples of basement rocks, with the results shown in Table 1. The minerals in those granites, sandstones and slates primarily include quartz, albite, microcline, muscovite, clinochlore and actinolite, with trace hematite in red shale. The granite (Pt-Gra) is mainly composed of quartz, albite and microcline and the

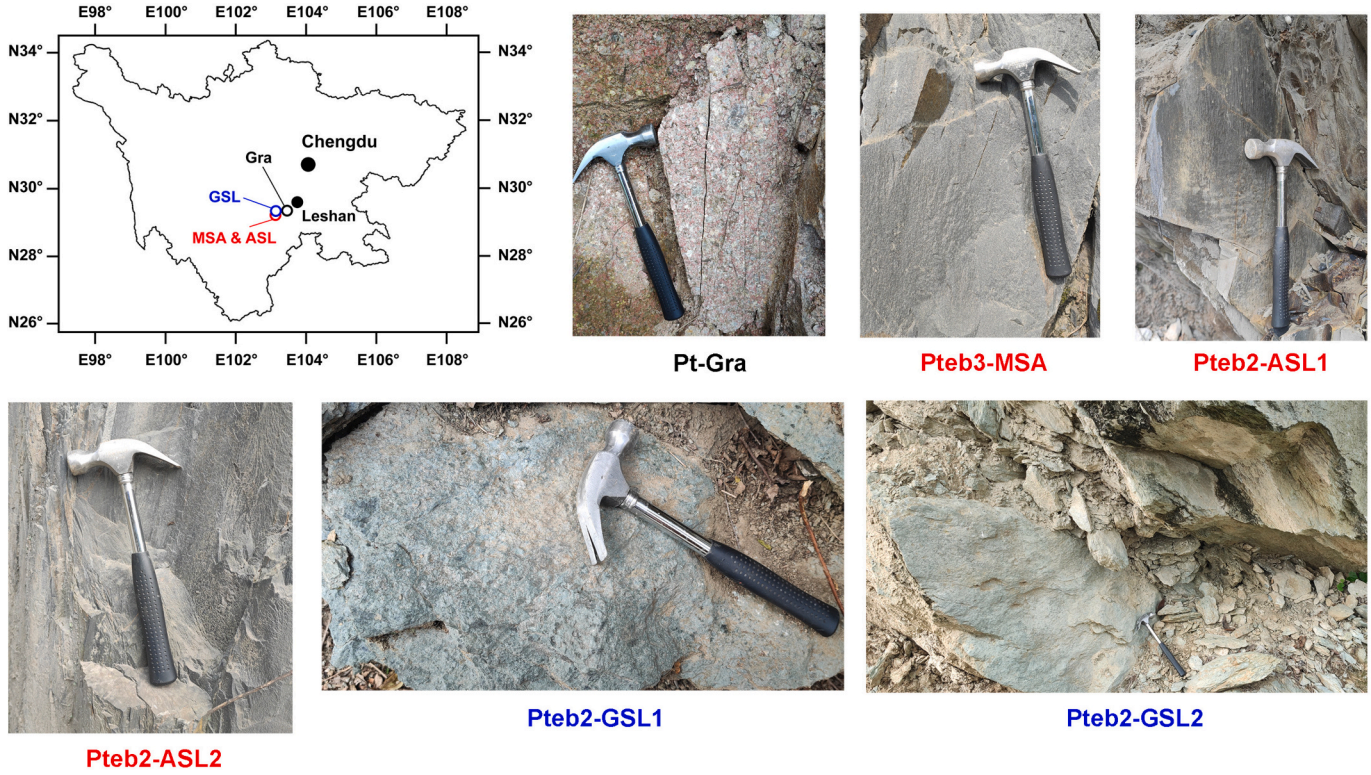

Fig. 3. Photos of the recovered Lower Proterozoic Granite (Pt-Gra) and Ebian Group (Pteb3-MSA, Pteb2-ASL1, Pteb2-ASL 2, Pteb2-GSL1, & Pteb2-GSL2) rocks from Leshan city, Sichuan Province. Nomenclature: Pt-Lower Proterozoic, eb3-Upper Ebian Group, eb2-Middle Ebian Group, Gra-Granite, MSA-Metasandstone, ASL-Argillaceous slate, GSL-Gray-green slate. The length of the geological hammer is 24 cm. (For interpretation of the references to colour in this figure legend, the reader is referred to the web version of this article.)

sandstone (Pteb3-MSA) in the Ebian Group show the highest proportion of quartz in these rocks, up to 75 wt%. Most of slates in the Ebian Group and Banxi Group are rich in clay minerals, with the clay proportions ranging from 25 to 70 wt%. Besides, the gray-green slates (Pteb2-GSL1 and Pteb2-GSL2) in the middle Ebian Group show a moderate proportion (23–41 wt%) of actinolite with no microcline be found in the Banxi Group slates.

As evident in many previous studies (An et al., 2020a; Kohli and Zoback, 2013; Tembe et al., 2010), the stability of natural or synthetic fault gouge material is primarily controlled by the proportion of clay (phyllosilicate). The clay-lean gouges tend to promote velocity-weakening response and unstable sliding. Hence, we choose six rocks with lower proportions of clays from Table 1 as representative to conduct the shear experiments, including samples Pt-Gra, Pteb3-MSA, Pteb2-GSL1, Ptbnf-GSL2, Ptbnt-SSL and Ptbnq-VSL. In the middle Ebian Group, the argillaceous slates were not chosen due to the very high contents of clay minerals (up to 70 wt%) and the sample Pteb2-GSL1 was adopted for shear experiments due to the higher proportions of actinolite (41 wt%) and clinochlore (38 wt%). The amphibole-rich gouges could exhibit unstable sliding at a low temperature and this moderate proportion of actinolite may also affect fault stability at basement temperatures and pressures (Fagereng and Ikari, 2020; Liu and He, 2020; Okamoto et al., 2020). After removing the surface impurities, the six selected basement rocks were crushed and sieved by pestle and mortar to <75 μm to simulate the fault gouges. The particle size distributions of the six selected gouges are shown in Fig. 5, with D10, D50 and D90 sizes listed in Table 2. The median particle diameters (D50) of the six rock gouges are primarily within the range 8–38 mm.

2.2. Experimental apparatus and procedures

The fault shear experiments were conducted using an argon-gas confined triaxial shear apparatus (He et al., 2006), with a schematic of the apparatus shown in Fig. 6a. Cylindrical gabbro blocks with diameters of 19.8 mm and heights of 40 mm were adopted as driving blocks cut at 35° along the axis to accommodate the fault gouge shear. The upper gabbro driving block was drilled with two holes for pore fluid channels and a dense brass filter inserted at the end of the holes to prevent gouge extrusion. The saw cut surfaces of the gabbro driving blocks were roughened by silicon carbide (SiC) abrasives to avoid shear slip. Our simulated gouge comprises two gabbro driving blocks sandwiching the inclined and embedded fault layer comprising ~1-mm-thick gouge and inserted into a 0.35-mm-thick annealed copper jacket before the shear experiments. High-hardness cylindrical tungsten carbide and corundum blocks and steel end plugs were placed at both ends of the copper jacket to support shear. Then, the copper jacket was inserted into a two-zone internal furnace and the space between the furnace and the copper jacket uniformly filled with boron nitride powders to prevent the gas convection. O-ring seals at both ends of the copper jacket seal the gouge with the high-pressure seal on the upper piston preventing escape of the argon gas and retaining the sealing of the entire assembly. A Teflon shim between the steel end plug and loading piston reduce frictional resistance. The inserted thermocouple was employed to measure the temperature at the mid-point of the gouge zone.

A total of six shear experiments were conducted on different rock gouges with clay contents of 4–45 wt% at a confining pressure of 110 MPa, a pore fluid pressure of 30 MPa, a temperature of 250 °C and slip velocities of 0.0488–0.244 μm/s, to assess the velocity dependence of frictional stability, with experimental details shown in Table 3. By assuming an average rock density of ~2400 kg/m^3 from those sedimentary layers and an equivalent buoyant density of 1400 kg/m^3 (representing hydrostatic loading) in Changning block of the Sichuan Basin (An et al., 2020b), the lithostatic and hydrostatic pressures at a depth of ~8 km are of the order of ~190 and ~ 110 MPa, respectively.

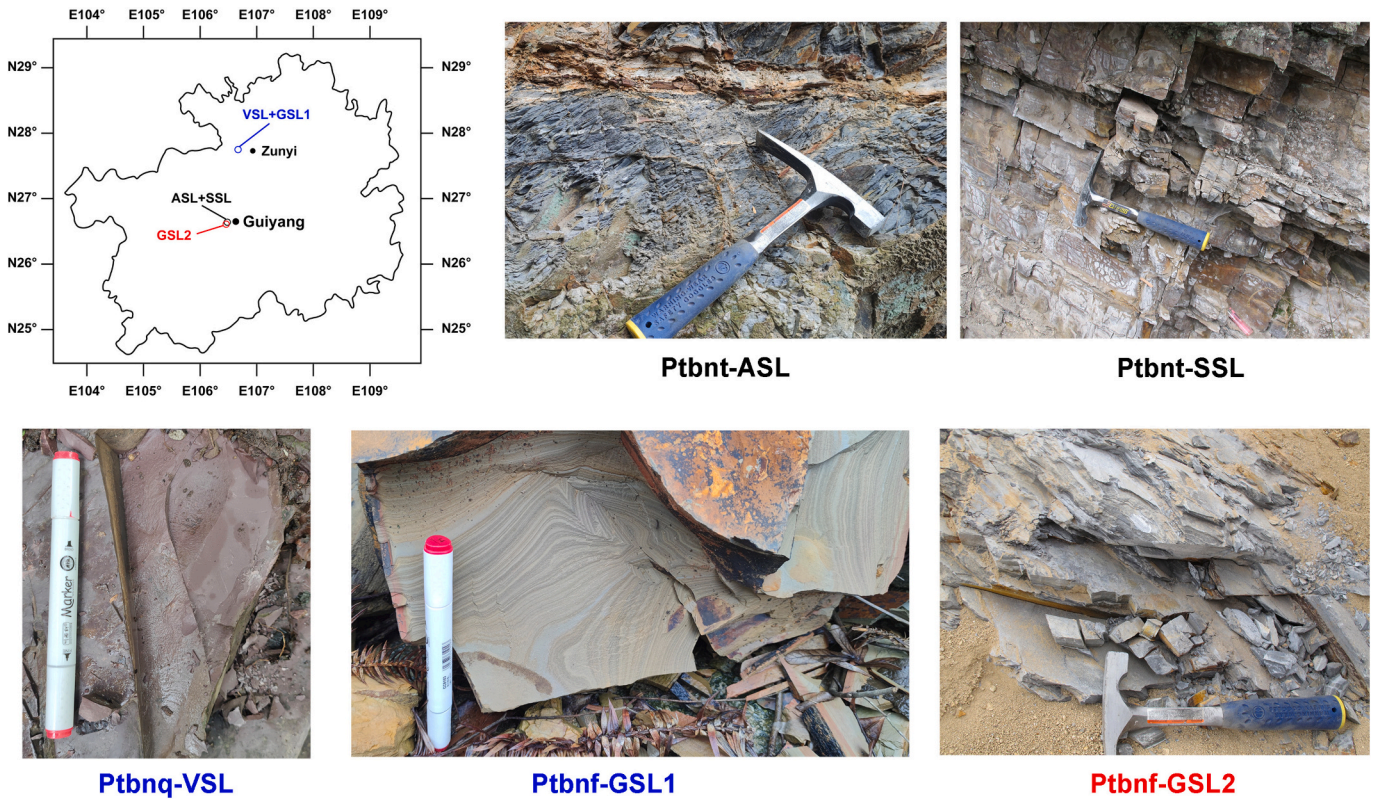

Fig. 4. Photos of the recovered Lower Proterozoic Banxi Group rocks (mostly slates) from Guiyang and Zunyi cities, Guizhou province. Nomenclature: Pt-Lower Proterozoic, bnt-Tiechang Formation in Banxi Group, bnq-Qingshuijiang Formation in Banxi Group, bnf-Fanzhao Formation in Banxi Group, ASL-Argillaceous slate, SSL-Sandy slate, VSL-Voiletish red slate, GSL-Gray-green or gray slate. The lengths of the geological hammer and gel pen are 28 and 15 cm, respectively. (For interpretation of the references to colour in this figure legend, the reader is referred to the web version of this article.)

Table 1
Recovered rocks and the corresponding mineral compositions in weight percent. Nomenclature: Gr.-Group, Fm.-Formation, Qtz-quartz, Alb-albite, Mic-microcline, Mus-muscovite, Cli-clinochlore, Act-Actinolite, Hem-hematite. The clay minerals primarily include muscovite and clinochlore.

Rock ID	Era/Group	Lithology	Mineral compositions (wt%)							
			Qtz	Alb	Mic	Mus	Cli	Act	Hem	**Clays**
Pt-Gra	Lower Proterozoic	Granite	52	24	20	3	1	–	–	**4**
Pteb3-MSA	Upper Ebian Gr.	Metasandstone	75	4	1	7	13	–	–	**20**
Pteb2-ASL1	Middle Ebian Gr.	Argillaceous slate	47	8	3	21	21	–	–	**42**
Pteb2-ASL2		Argillaceous slate	18	8	4	45	25	–	–	**70**
Pteb2-GSL1		Gray-green slate	6	–	11	4	38	41	–	**42**
Pteb2-GSL2		Gray-green slate	21	9	6	10	31	23	–	**41**
Ptbnt-ASL	Tiechang Fm., Banxi Gr.	Argillaceous slate	41	9	–	48	2	–	–	**50**
Ptbnt-SSL		Sandy slate	62	13	–	20	5	–	–	**25**
Ptbnq-VSL	Qingshuijiang Fm., Banxi Gr.	Voiletish red slate	45	11	–	34	5	–	5	**39**
Ptbnf-GSL1	Fanzhao Fm., Banxi Gr.	Gray-green slate	54	–	–	40	6	–	–	**46**
Ptbnf-GSL2		Gray slate	43	12	–	39	6	–	–	**45**

We use these lithostatic and hydrostatic pressures as the confining and pore fluid pressures, respectively, for the tri-axial shear tests. We adopt a confining pressure of ~110 MPa and a pore fluid pressure of ~30 MPa to represent the equivalent in-situ effective stress (an effective confining stress of ~80 MPa) and controlling deformation response at a depth of ~8 km. The thermal gradient in the southeastern Sichuan basin approaches 30 °C/km with the earth surface temperature assumed to be ~10 °C (An et al., 2020b). The in-situ temperature at a depth of ~8 km therefore approaches ~250 °C. In sum, the testing conditions correspond to the in-situ effective stress and temperature at a depth of ~8 km.

Confining and pore fluid pressures were elevated to half of the desired values at the initiation of each shear test. Deionized water was adopted as the pore fluid to minimize the chemical effects. Then, the temperature was elevated to the desired value at a rate of 5 °C/min followed by elevating the confining and pore fluid pressures to the desired values. Accuracies of the confining and pore fluid pressure were controlled to be ±0.3 and 0.1 MPa, respectively. During the tests, the gouges were initially sheared at a slip rate of 1.22 μm/s to steady state friction with the slip rates then incremented or decremented between 1.22, 0.244 and 0.0488 μm/s (corresponding to axial velocities of 1.0, 0.2 and 0.04 μm/s) to explore the velocity dependence of friction. Slip displacements at slip rates of 1.22 and 0.244 μm/s were designed to be 0.366 mm, but decreased to 0.244 mm at the lowest slip rate of 0.0488 μm/s. Axial load and displacements were recorded by a high-precision load cell and displacement sensor at a sampling frequency of 1 Hz. Temperature during the test was recorded and controlled by a temperature controller to an accuracy of ±2 °C.

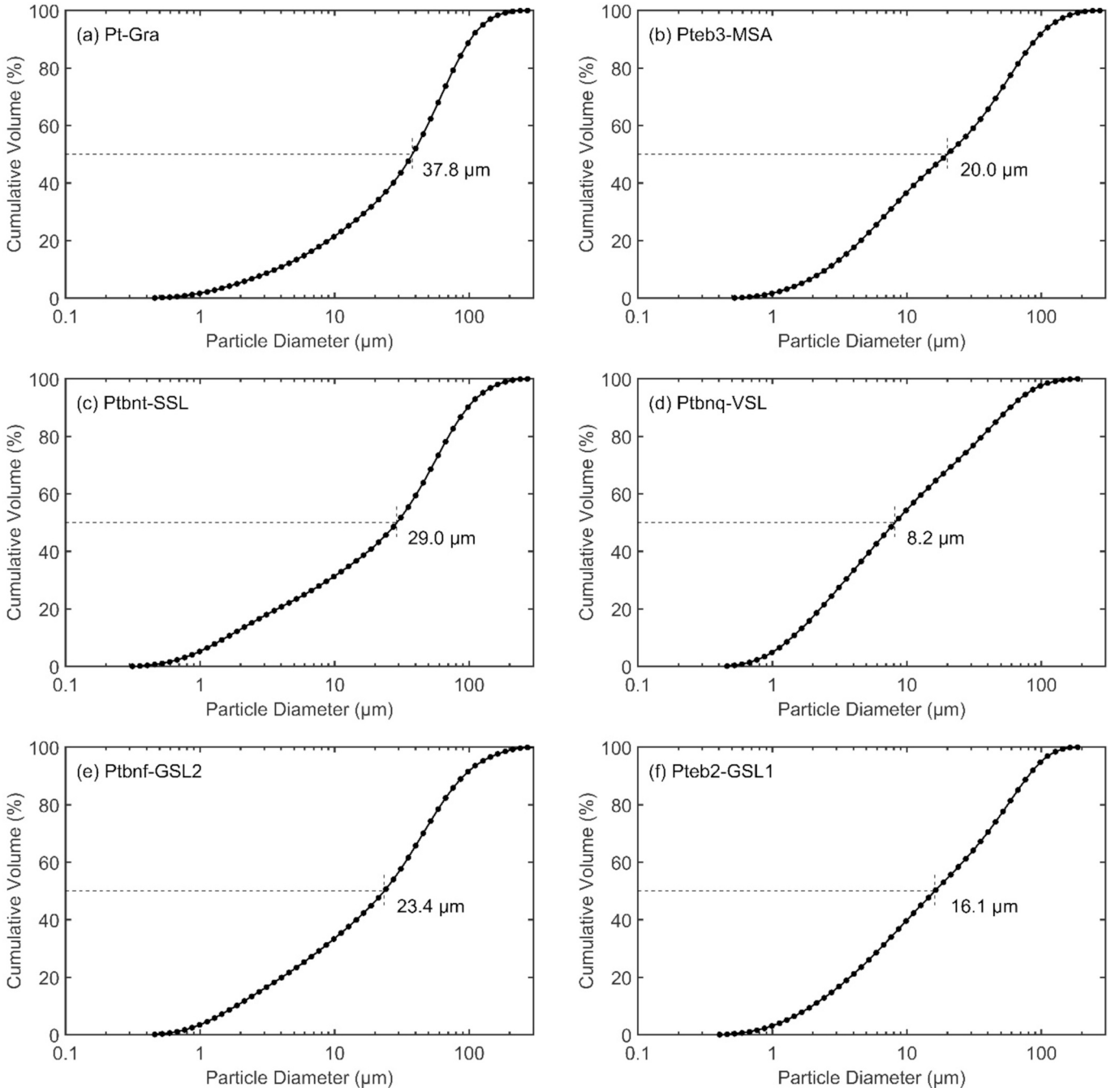

Fig. 5. The particle size distributions of the six selected rock gouges with the median particle sizes marked, (a) Pt-Gra, (b) Pteb3-MSA, (c) Ptbnt-SSL, (d) Ptbnq-VSL, (e) Ptbnf-GSL2, and (f) Pteb2-GSL1.

Table 2
Particle diameters corresponding to D10, D50 and D90 of the six selected rock gouges. D10, D50 and D90 indicate 10, 50 and 90 vol% particle size less than this diameter.

Gouges	Pt-Gra	Pteb3-MSA	Ptbnt-SSL	Ptbnq-VSL	Ptbnf-GSL2	Pteb2-GSL1
D10 (μm)	3.6	2.5	1.5	1.4	1.9	2.0
D50 (μm)	37.8	20.0	29.0	8.2	23.4	16.1
D90 (μm)	102.7	91.1	97.6	58.4	91.0	79.7

2.3. Experimental data calculations

The raw experimental data, including the axial load, axial displacement, temperature, confining and pore fluid pressures are used according to He et al. (2006). The raw experimental data are corrected due to the variation in gouge contact area with increasing shear displacement and the shear resistance form the copper jacket. The equations used for calibrating the varying contact areas are described in He et al. (2006). The equivalent shear resistance of the copper jacket is measured from the steel driving blocks sandwiched by the Teflon shim. The fault frictional strength, i.e., the coefficient of friction (μ), was calculated following Amontons' law, as,

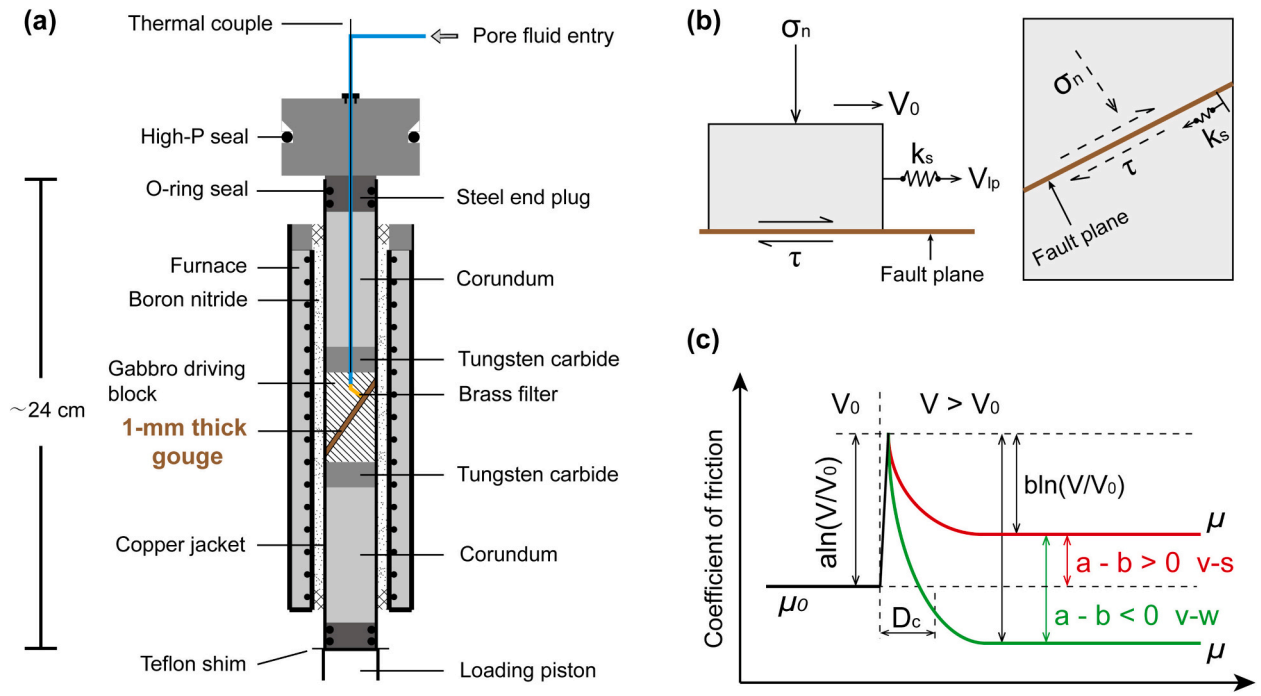

Fig. 6. (a) Schematic of triaxial shear assembly. (b) Conceptual sliding model representing fault slip behavior. (c) Idealized frictional response of velocity-strengthening (*v-s*) and velocity-weakening (*v-w*) at an incremented velocity step.

Table 3
Experiment details. Nomenclature: σ_c-confining pressure, P_f-pore fluid pressure, V-slip velocity, L_t-total shear displacement, *v-s*-velocity-strengthening behavior, *v-w*-velocity-weakening behavior, *s-s*-stick-slip behavior.

Gouge	σ_c (MPa)	P_f (MPa)	T (°C)	V (μm/s)	L_t (mm)	V dependence
Pt-Gra	110	30	250	1.22–0.244-0.0488	3.81	*v-w*, *s-s*
Pteb3-MSA	110	30	250	1.22–0.244-0.0488	3.81	*v-w*, s-s
Pteb2-GSL1	110	30	250	1.22–0.244-0.0488	3.99	*v-s*
Ptbnf-GSL2	110	30	250	1.22–0.244-0.0488	3.77	*v-s*
Ptbnt-SSL	110	30	250	1.22–0.244-0.0488	3.69	*v-s*, *v-w*
Ptbnq-VSL	110	30	250	1.22–0.244-0.0488	3.51	*v-s*

$$\mu = \frac{\tau_c}{\sigma_n - P_f} = \frac{\tau_c}{\sigma_{neff}} \tag{1}$$

where τ_c is the corrected shear stress, σ_n, P_f and σ_{neff} are the applied normal stress, pore fluid pressure and effective normal stress, respectively. The fault frictional velocity dependence is calculated using rate-and-state friction (RSF) based on a simple spring-slider model (Dieterich, 1979; Ruina, 1983; Gu et al., 1984; Marone, 1998) (Fig. 6b). RSF theory describes the evolution of fault coefficient of friction with a change in shear velocity and provides a connection between the velocity dependence of friction. The most frequently employed RSF law is the Dieterich or Ruina evolution laws with the expression of,

$$\mu = \mu_0 + a\ln\left(\frac{V}{V_0}\right) + b\ln\left(\frac{V_0\theta}{D_c}\right) \tag{2}$$

$$\frac{d\theta}{dt} = 1 - \frac{V\theta}{D_c} \text{ (Dieterich evolution law)} \tag{3}$$

$$\frac{d\theta}{dt} = -\frac{V\theta}{D_c}\ln\left(\frac{V\theta}{D_c}\right) \text{ (Ruina evolution law)} \tag{4}$$

where μ_0 is a steady-state coefficient of friction at a prior slip rate V_0, V is the current fault frictional slip rate, D_c represents the slip necessary to renew the fault surface contacts, i.e., the critical slip displacements necessary from a past steady-state to a new steady-state, a and b are two dimensionless constants that describe the direct or evolutional effects upon an upward velocity step, θ is defined as the ratio of D_c/V and represents the average contact lifetime. Fault frictional slip stability may be determined by the parameter $(a-b)$ derived from Eqs. (2) and (3) or Eqs. (2) and (4) at a single velocity step, yielding,

$$a - b = \frac{\Delta\mu_{ss}}{\Delta \ln V} \tag{5}$$

where $\Delta\mu_{ss}$ represents the difference in coefficients of friction before and after a velocity step. Positive values of $(a-b)$ indicate an increased coefficient of friction after an incremented velocity upstep and denotes velocity-strengthening behavior, indicative of inherently stable and aseismic slip response. Conversely, a negative value of $(a-b)$ represents a decreased coefficient of friction after an incremented velocity upstep and denotes velocity-weakening behavior. A negative value of $(a-b)$ is a necessary prerequisite for fault instability. Faults with negative values of $(a-b)$ indicate unstable sliding whenever the fault critical stiffness is also met (Gu et al., 1984). Idealized responses of velocity-strengthening or velocity-weakening at an upward velocity step are shown in Fig. 6c. Potential experimental measurement errors are primarily sourced from the calibrations of the experimental data, the measurements of the coefficients of friction and the calculations of frictional stability parameters $(a-b)$. The errors due to the experimental data calibrations are primarily the equivalent shear resistance from the copper jacket - we generally measure the equivalent shear resistance at least three times and take the average value to minimize the error. The measurements of the coefficients of friction also produce errors due to the background noise at the lower velocities of 0.244 and 0.0488 μm/s but this error is generally below ±0.05. The errors in calculating the frictional stability

parameters ($a-b$) are sourced from detrending the slope but this error is below ±0.0005.

2.4. Fluid injection model setup

We define magnitudes of poroelastic stress perturbations resulting from injection into three prismatic injection zones, as depicted in Fig. 7. The models honor typical injection zone configurations in the Sichuan Basin of southwest China by combing the adjacent fracturing clusters into the same fracturing zone (An et al., 2021; Chen et al., 2018; Zhang et al., 2019a). Although the compositions of Longmaxi shales in Sichuan Basin are highly variable (An et al., 2020a), we assume that the fluid injection is completed in the isotropic, porous and elastic shale layers at a burial depth of 3000 m. This depth is consistent with current shale gas extraction zone in the Changning, Weiyuan and Luzhou blocks in the southeast Sichuan Basin (An et al., 2021). The elastic modulus (E) and Poisson's ratio (ν) are taken as 40 GPa and 0.20, respectively. Each prismatic injection zone is 1500 m (length) × 400 m (width) × 200 m (height), with the injection point (i.e., the heel of the injection well) located at the center of the prismatic zone. The injection zone spacing is 500 m with fluid injection operated for all three zones simultaneously – this condition corresponds to the most disruptive case. The origin of the coordinate system is located at the center of the injection zone, with the x, y, and z axes along the length, width and height directions of those injection zones.

We explore influences from the magnitudes of the pore pressure increase (ΔP) and the distance (d) between the evaluation plane and the injection zone. It is assumed that there is no fluid leak-off and the pore fluid pressure increase is uniform across the injection zones. Under this condition, the effect from pore pressure increase is equivalent to the increase in injected fluid volume. Consequently, the pore fluid pressure continuously increases upon increasing the injected fluid volume and we assume the pore fluid pressure changes (ΔP) are 5, 10, and 15 MPa in our simulations. At the highest pore pressure change (i.e., $\Delta P = 15$ MPa), the pore fluid pressure at a burial depth of 3000 m would be x1.5 that of hydrostatic pressure. All the above simulations and calculations were performed using MATLAB.

It should be noted that the current numerical model still has several limitations compared to the poroelastic plane strain model and the finite difference or finite element method by Chang and Segall, 2016a, 2016b, Lei et al. (2017) and Fan et al. (2019). The multilayered two-dimensional plane-strain model proposed by Chang and Segall (2016a, 2016b) incorporated the effects of reservoir strata heterogeneity and fault geometry to quantify magnitudes of Coulomb failure stress from both direct pore pressure increase and poroelastic effects. Meanwhile, rate- and -state friction theory was also implemented in the model to differentiate the velocity-dependent behaviors. Lei et al. (2017) adopted the coupled "TOUGH-FLAC" approach to simulate the changes of Coulomb failure stress due to hydraulic fracturing for varied fault strikes, dips and rakes and different fluid injection volumes and rates. Fan et al. (2019) employed the three-dimensional finite element models to further explore the fault zone permeability structures based on the fault core permeability models proposed by Caine et al. (1996). Our simplified model currently does not incorporate the effects of multiple fluid injection parameters nor strata heterogeneity and complex geometry. The model also does not define stress evolution at a longer time scale. However, this simplified model does provide a rapid estimation of the magnitudes of induced poroelastic stresses based on the limited input parameters of pore pressure change, injection zone dimensions and unified rock mechanical parameters. Although the uniformity of pore pressures increase is typically not applicable in field fluid injection engineering, this is a common assumption adopted by numerous models, including the above poroelastic plane strain and coupled "TOUGH-FLAC" models (Chang and Segall (2016a, 2016b), Lei et al. (2017)). Besides, our model considers the effects of the magnitudes of pore pressure increase to partially compensate for the nonuniform pore pressure increase in field application.

2.5. Governing equations

The governing equations for calculating the stresses induced in a pressurized prismatic zone are based on the methods described in Okada (1992) (inflation type). For a prismatic injection zone, the corresponding displacement $u(x, y, z)$ due to the pore fluid pressure increase is expressed as,

$$u(x,y,z) = \frac{M_0}{2\pi\mu}\left[u_A(x,y,z) - u_A(x,y,-z) + u_B(x,y,z) + zu_c(x,y,z)\right] \quad (6)$$

$$M_0 = \alpha \bullet \Delta P \quad (7)$$

where α is the Biot coefficient and assumed to be 0.6 (Zoback, 2007), and ΔP represents the increase in pore fluid pressure. The displacement components u_A, u_B, and u_C are then calculated as,

$$u_{Ax} = \frac{x(\beta-1)}{2R^3}, u_{Ay} = \frac{y(\beta-1)}{2R^3}, u_{Az} = \frac{D(\beta-1)}{2R^3} \quad (8)$$

$$u_{Bx} = \frac{x(1-\beta)}{\beta R^3}, u_{By} = \frac{y(1-\beta)}{\beta R^3}, u_{Bz} = \frac{D(1-\beta)}{\beta R^3} \quad (9)$$

$$u_{Cx} = \frac{3xD(1-\beta)}{R^5}, u_{Cy} = \frac{3yD(1-\beta)}{R^5}, u_{Cz} = \frac{\left(R^2-3D^2\right)(1-\beta)}{R^5} \quad (10)$$

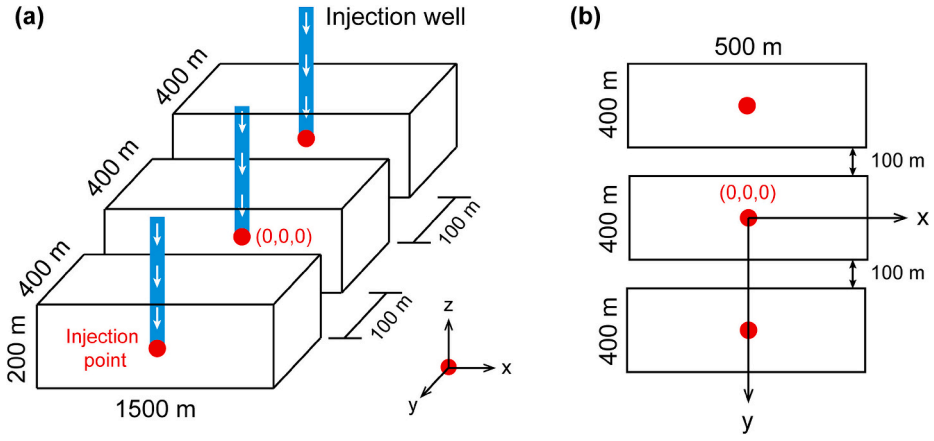

Fig. 7. Schematic for injection in three prismatic injection zones: (a) 3D view, (b) plan view (XY plane). The cyan footprints and red circles represent the injection wells and injection points, respectively. (For interpretation of the references to colour in this figure legend, the reader is referred to the web version of this article.)

$$D = c - z, R^2 = x^2 + y^2 + z^2, \beta = \frac{\lambda + \mu}{\lambda + 2\mu} \tag{11}$$

where c represents the depth of the injection zone, and λ and μ are the two Lamé constants. The six strain components ε_{xx}, ε_{yy}, ε_{zz}, ε_{xy}, ε_{xz}, and ε_{yz} in the pressurized prismatic zone are calculated as,

$$\varepsilon_{xx} = u_{xx}, \varepsilon_{yy} = u_{yy}, \varepsilon_{zz} = u_{zz}, \varepsilon_v = \varepsilon_{xx} + \varepsilon_{yy} + \varepsilon_{zz} \tag{12}$$

$$\varepsilon_{xy} = \frac{u_{xy} + u_{yx}}{2}, \varepsilon_{xz} = \frac{u_{xz} + u_{zx}}{2}, \varepsilon_{yz} = \frac{u_{yz} + u_{zy}}{2} \tag{13}$$

and finally, the six stress components σ_{xx}, σ_{yy}, σ_{zz}, σ_{xy}, σ_{xz}, and σ_{yz} due to pore fluid pressure increase in the prismatic zone are calculated as,

$$\sigma_{xx} = \lambda\varepsilon_v + 2\mu\varepsilon_{xx}, \sigma_{yy} = \lambda\varepsilon_v + 2\mu\varepsilon_{yy}, \sigma_{zz} = \lambda\varepsilon_v + 2\mu\varepsilon_{zz} \tag{14}$$

$$\sigma_{xy} = 2\mu\varepsilon_{xy}, \sigma_{xz} = 2\mu\varepsilon_{xz}, \sigma_{yz} = 2\mu\varepsilon_{yz} \tag{15}$$

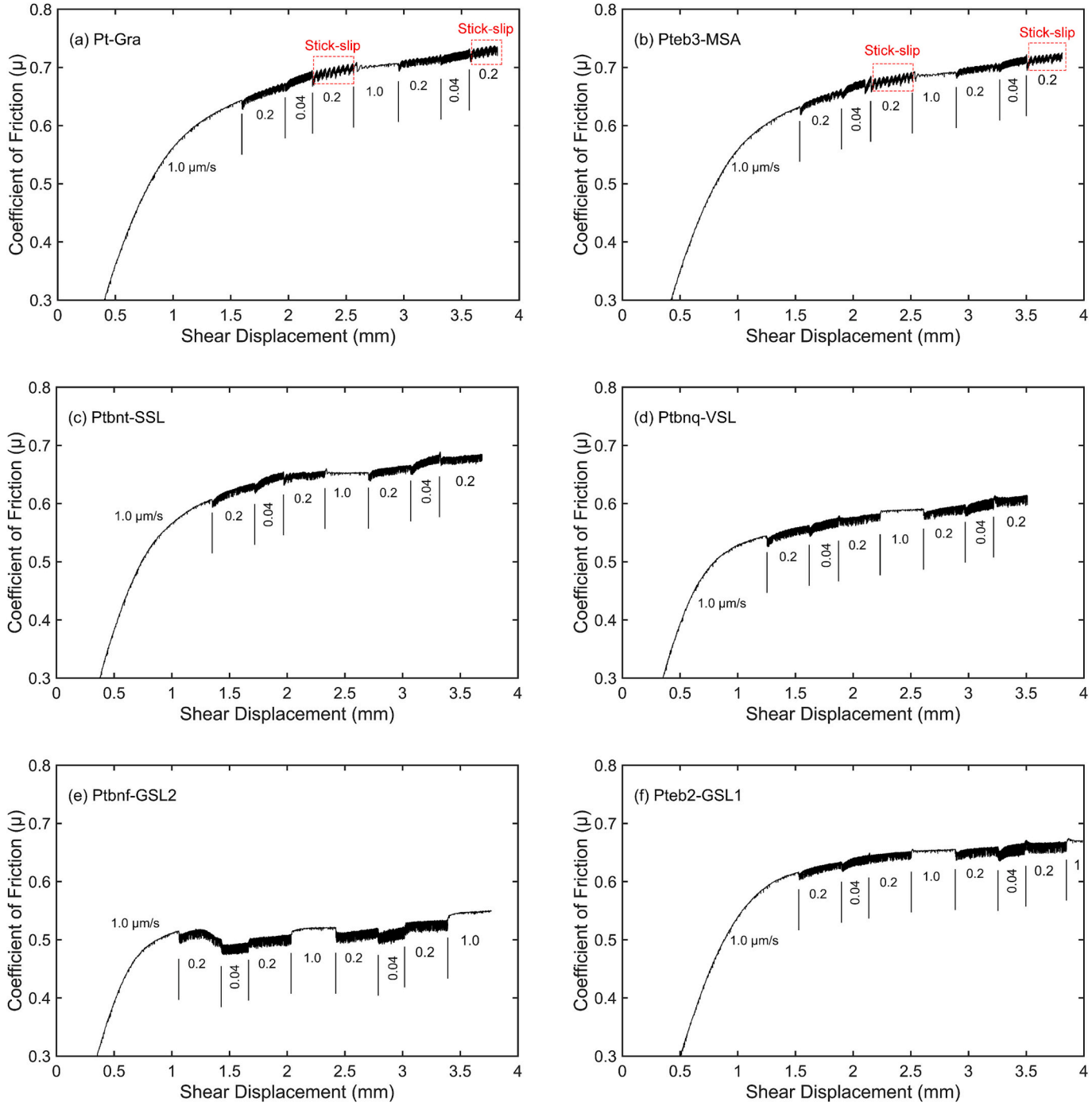

Fig. 8. Evolution of fault coefficient of friction with increasing shear displacements for the six rock gouges, (a) Pt-Gra, (b) Pteb3-MSA, (c) Ptbnt-SSL, (d) Ptbnq-VSL, (e) Ptbnf-GSL2, and (f) Pteb2-GSL1. Axial slip velocities are marked below the curves and the red dashed squares in panels (a) and (b) indicate the stick-slip behaviors. (For interpretation of the references to colour in this figure legend, the reader is referred to the web version of this article.)

3. Results

3.1. Friction/stability at higher temperatures

The variations of coefficients of friction with increasing shear displacements for the six rock gouges at $\sigma_c = 110$ MPa, $P_f = 30$ MPa and $T = 250$ °C are shown in Fig. 8. All gouges exhibit a linear increase in friction within the initial 1.0 mm of shear displacement, followed by macroscopic yield and then strain-strengthening responses at shear displacements of 1.0–4.0 mm. In most cases, the six rock gouges show only stable sliding but minor stick-slips can be observed the slip rates of 0.244 μm/s for gouges Pt-Gra and Pteb3-MSA (Fig. 8a-b). The stick-slips also indicate the potential for seismic response according to Brace and Byerlee (1966).

Frictional strengths of the six rock gouges are primarily within the range 0.5–0.7 with a decreasing trend of frictional strength with increasing clay (phyllosilicate) contents observed, except for gouge Pteb2-GSL1 (42 % clays) (Fig. 9a and Table 4). This trend is broadly consistent with many studies where the increase in clay contents lower gouge frictional strength (Tembe et al., 2010; Kohli and Zoback, 2013; Fang et al., 2018; Zhang et al., 2019b; An et al., 2020a). The higher frictional strength in rock gouge Pteb2-GSL1 may result from higher contents of actinolite (41 *wt*%) and clinochlore (38 *wt*%). The amphibolite minerals are also frictionally-strong minerals (μ ≈ 0.7) with frictional strengths similar to those for quartz or feldspar gouges with the frictional strength of pure clinochlore gouge also higher (up to 0.4–0.5) than most common clay minerals (0.2–0.3) under hydrothermal conditions (He et al., 2013; Okamoto et al., 2019; Fagereng and Ikari, 2020; Liu and He, 2020; Belzer and French, 2022). Following the methods described in Section 2.3, frictional stability, i.e., values of $(a - b)$ are calculated from the results shown in Fig. 9b and Table 4. Apparently, a transition from velocity-weakening ($a - b < 0$) to velocity-strengthening ($a - b > 0$) is observed with increasing clay (phyllosilicate) contents, indicating the destabilizing effect for gouges with lower clay contents. These negative values of $(a - b)$, paired with higher frictional strength are inconsistent with the relation of fault strength and frictional stability reported by Ikari et al. (2011). However, the transitional clay content (~40 *wt*%) in our study is typically higher than that at room temperature due to the destabilizing effect from the high testing temperature ($T = 250$ °C) (Kohli and Zoback, 2013; Zhang et al., 2019b).

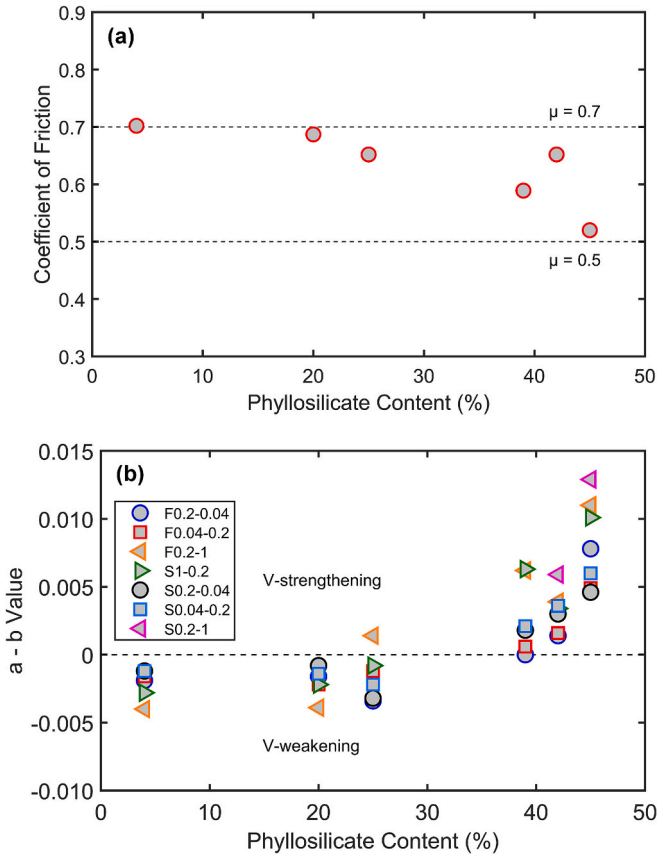

Fig. 9. (a) Fault coefficient of friction (μ) and (b) stability ($a - b$) versus phyllosilicate (clay) content for the six rock gouges. The two dashed lines in panel (a) represent $\mu = 0.5$ and 0.7, respectively. The legend in panel (b) indicates the velocity steps.

3.2. Poroelastic stresses induced by fluid injection

Following the methods described in Sections 2.4 and 2.5, we calculated the induced poroelastic stresses from three prismatic injection zones, with contours of induced poroelastic stresses at $\Delta P = 15$ MPa and $d = 2$ km shown in Fig. 10. Our sign convention is positive in compression. Compression zones were formed around the injection location for both σ_{xx} and σ_{yy} (Fig. 10a-b) with extension for σ_{zz} (Fig. 10c). For the stress component σ_{xy}, the compression and extension zones develop along the diagonal (Fig. 10d), but they show the left-right and top-bottom distributions in the stress components σ_{xz} and σ_{yz}, respectively (Fig. 10e-f).

From Fig. 10, the magnitudes of the induced poroelastic stresses resulting from the three prismatic fluid injection zones at a distance of $d = 2$ km could reach ~10^{-2} MPa, similar to those values from the multistage hydraulic fracturing (30 stages) (An et al., 2021). However, the magnitudes of induced poroelastic stresses decay rapidly with increasing distances. The magnitudes of the highest poroelastic stresses in σ_{xx}, σ_{yy}, and σ_{zz} along either the *x*- or *y*- axes are higher than 10^{-2} MPa at $d = 2$ km, but decrease to 10^{-3}–10^{-2} MPa at $d = 3$ km and 10^{-4}–10^{-3} MPa at $d = 4$ and 5 km (Fig. 11a-c and S2a-S2c). The magnitudes of the highest poroelastic stress for the stress components σ_{xy} along $x = -1000$ m or $y = -1000$ m and σ_{yz} along $x = -1000$ m also decrease from 10^{-3} MPa at $d = 2$ and 3 km to 10^{-4} MPa at $d = 4$ and 5 km (Fig. 11d, S2d and S2f). The magnitudes of the highest poroelastic stress for the stress components σ_{xz} and σ_{yz} along the *x*- or *y*- axis also decrease from 10^{-2} MPa at $d = 2$ km to 10^{-3} MPa at $d = 3$ and 4 km and 10^{-4} MPa at $d = 5$ km (Fig. 11e-f and S2e). In addition, the poroelastic stresses in the stress components σ_{xx}, σ_{yy}, and σ_{zz} at $d = 2$ km also show sharp decreases from $>10^{-2}$ MPa at the central injection point to 10^{-3} MPa at the edge of the zone, further showing the rapid stress decay with increasing distance (Fig. 11a-c). This trend is also consistent with the results of Lei et al. (2017) that the injection induced poroelastic stress changes are higher than ~0.3 MPa around the injection zone but decrease to <0.1 MPa at a distance greater than 1 km. These influences are also apparent in the governing equations in Section 2.5. As the distances directly affect the magnitudes of the displacement components u_A, u_B and u_C, they further affect the magnitudes of displacements $u(x, y, z)$ and the six stress components. Decreasing the pore pressure change also lowers the magnitudes of induced poroelastic stresses (Fig. 12 and S3) with the stress reduction proportional to the pore pressure change according to Eqs. (6)–(7). In addition, the decay of poroelastic stresses from the pore pressure change is less significant at increasing distances.

A common method to evaluate the effect of poroelastic stress perturbations on deep fault stability is by calculating the Coulomb failure stress (*CFS*) (Sumy et al., 2014; Kettlety et al., 2019; Goebel et al., 2017), defined as,

$$\Delta CFS = \Delta\tau - \mu_s \bullet \left(\Delta\sigma_n - \Delta P_f\right) = \Delta\tau - \mu_s \bullet \Delta\sigma_{neff} \tag{16}$$

where ΔCFS, $\Delta\tau$, $\Delta\sigma_n$, ΔP_f, and $\Delta\sigma_{neff}$ represent the changes in Coulomb failure stress, shear stress, normal stress, pore fluid pressure and effective normal stress, respectively. μ_s is the static coefficient of friction of preexisting faults and assumed to be 0.6. Based on Eq. (16), the

Table 4
Results of frictional strength (μ_{ss}) and stability ($a-b$) for the six rock gouges. The frictional strengths (μ_{ss}) were measured at a shear displacement of ~2.5 mm and an axial velocity of 1.0 μm/s. Nomenclature: F-First, S- Second, and they indicate the sequence of velocity-steps.

Rock gouges	μ_{ss}	Values of ($a-b$) at different axial velocities (μm/s)						
		F0.2–0.04	F0.04–0.2	F0.2–1.0	S1.0–0.2	S0.2–0.04	S0.04–0.2	S0.2–1.0
Pt-Gra	0.702	−0.0019	−0.0016	−0.0040	−0.0028	−0.0012	−0.0012	–
Pteb3-MSA	0.687	−0.0016	−0.0022	−0.0039	−0.0022	−0.0008	−0.0014	–
Ptbnt-SSL	0.652	−0.0034	−0.0012	0.0014	−0.0008	−0.0032	−0.0022	–
Ptbnq-VSL	0.589	0	0.0006	0.0062	0.0063	0.0018	0.0021	–
Ptbnf-GSL2	0.520	0.0078	0.0049	0.0110	0.0101	0.0046	0.0060	0.0129
Pteb2-GSL1	0.652	0.0014	0.0016	0.0039	0.0034	0.0030	0.0036	0.0059

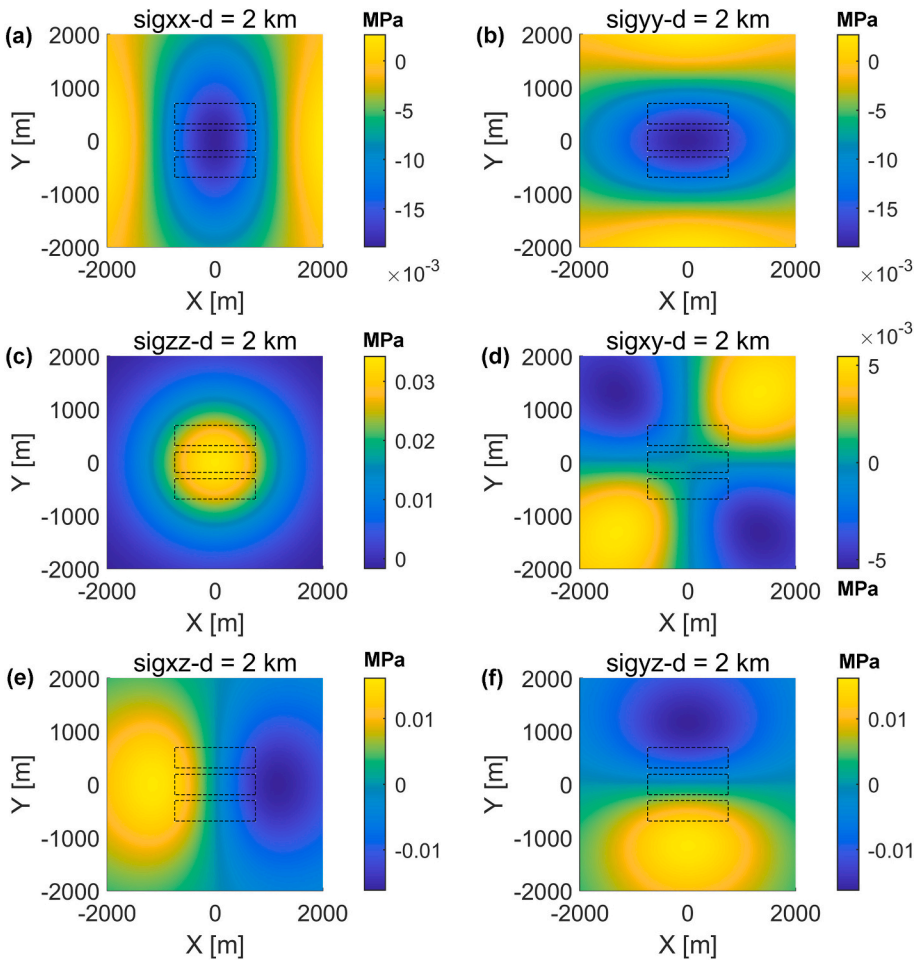

Fig. 10. Contours of induced poroelastic stresses at $d = 2$ *km* and $\Delta P = 15$ *MPa* due to three prismatic injection zones (dashed black rectangles). Panels (a)-(f) represent the contours of the six stress components σ_{xx}, σ_{yy}, σ_{zz}, σ_{xy}, σ_{xz} and σ_{yz}, respectively.

preexisting faults could be reactivated by positive ΔCFS values and the threshold ΔCFS values to trigger seismicity could be as low as 0.01 MPa (Harris, 1998; Stein, 1999).

To calculate the induced ΔCFS values, we assume a series of preexisting faults with strike along the positive y axis, dip along the positive x axis and dip angles of 15°, 30°, 45°, and 60°. The results of ΔCFS values at different distances ($d = 2$, 3, 4, and 5 km) are shown in Fig. 13. Only the ΔCFS values at $d = 2$ km could be higher than 10^{-2} MPa, and the values are primarily within 10^{-3} MPa at $d = 3$–4 km and 10^{-4} MPa at $d = 5$ km. These demonstrate that the fluid injection at a single fluid injection site comprising three adjacent prismatic zones could reactivate the critically-stressed fault at distances within 2 km.

4. Discussion

4.1. Basement seismic potential in the Southeastern Sichuan basin

Our fault gouge experiments show a strong correlation between the fault frictional strength/stability and mineralogical compositions. Fault frictional strength and instability are both be enhanced at lower phyllosilicate contents (Fig. 9). These results are in accordance with numerous studies focusing on either natural or synthetic gouges comprising assemblages of three mineral groups, i.e., the tectosilicates, carbonates and phyllosilicates (Tembe et al., 2010; Ikari et al., 2011; Kohli and Zoback, 2013; Zhang and He, 2013; Fang et al., 2018; Zhang et al., 2019b; An et al., 2020a). The tectosilicate-rich (including the quartz and feldspar) faults typically exhibit high frictional strength and are prone to show velocity-weakening and stick-slip behaviors at low-to-

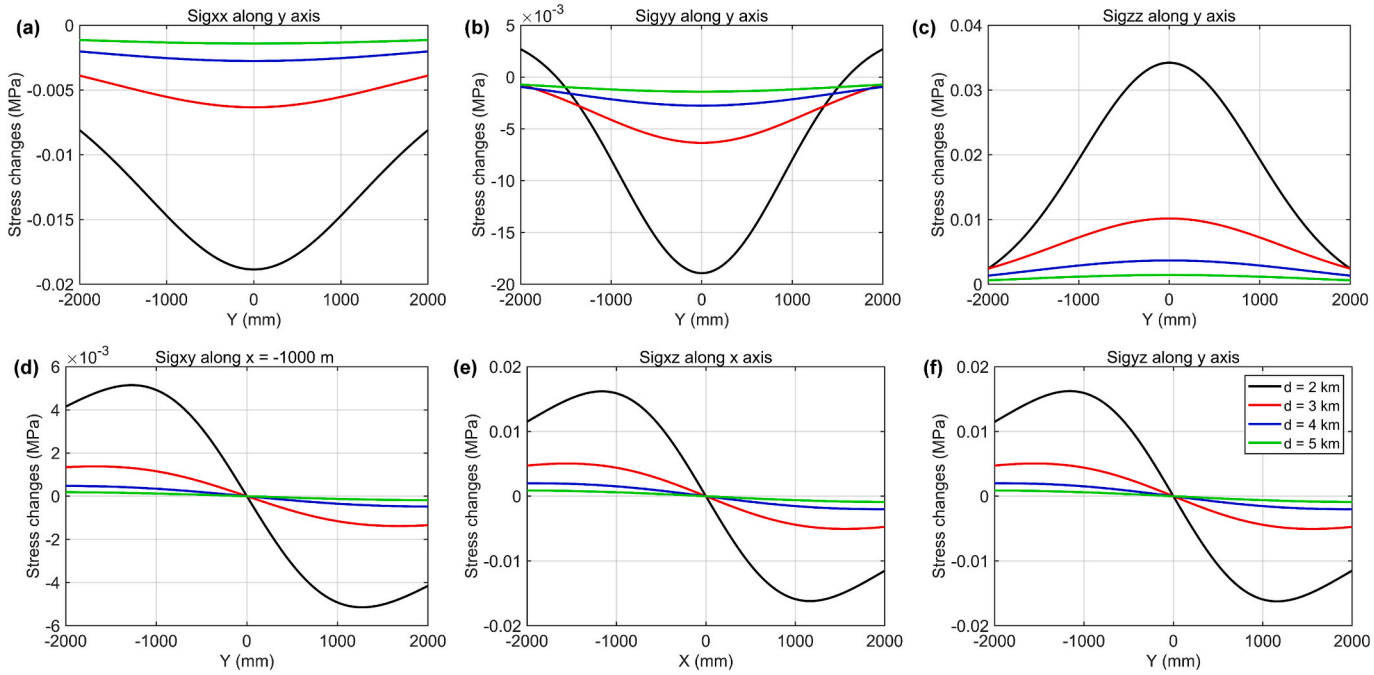

Fig. 11. Comparisons of induced poroelastic stresses at $\Delta P = 15$ MPa and different distances ($d = 2$, 3, 4, and 5 km) due to three prismatic pressurized injection zones, (a) Stress changes of σ_{xx} along the y axis, (b) Stress changes of σ_{yy} along the y axis, (c) Stress changes of σ_{zz} along the y axis, (d) Stress changes of σ_{xy} along $x = -1000$ m, (e) Stress changes of σ_{xz} along the x axis, and (f) Stress changes of σ_{yz} along the y axis.

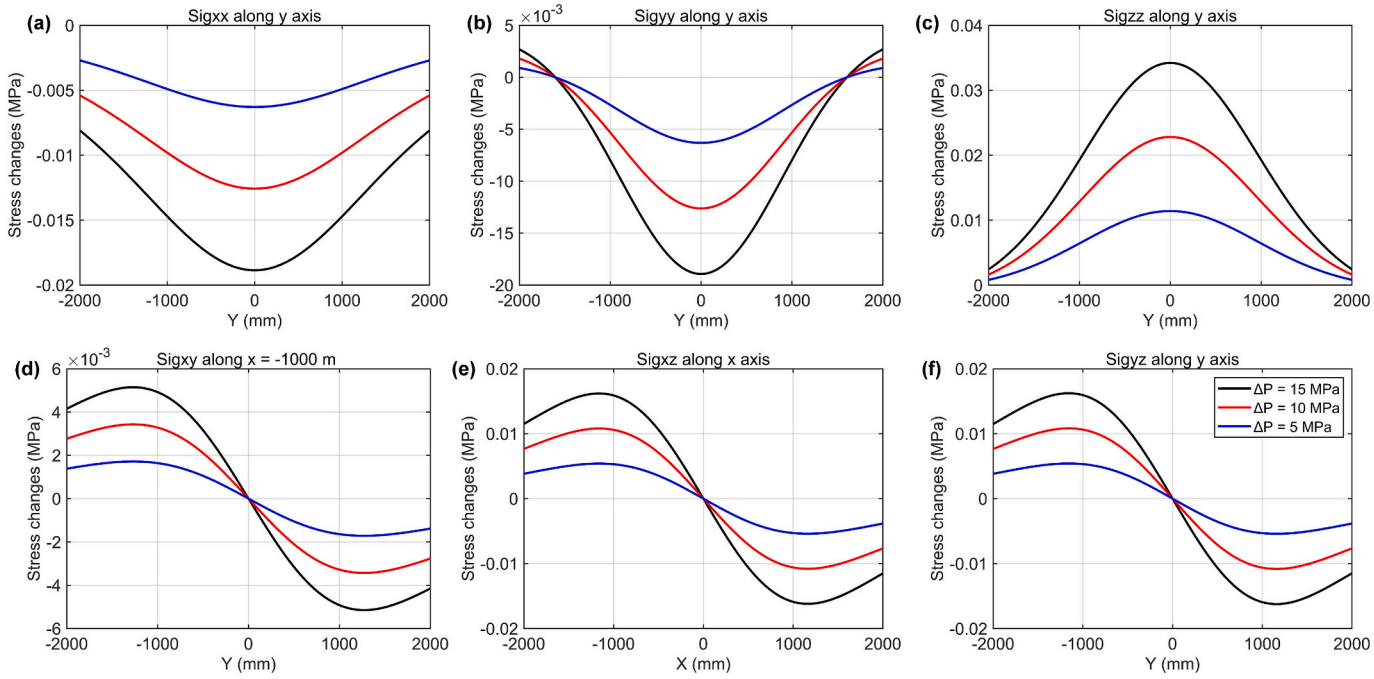

Fig. 12. Comparisons of induced poroelastic stresses at $d = 2$ km for different pore pressure changes ($\Delta P = 5$, 10, and 15 MPa) due to three prismatic pressurized injection zones, (a) Stress changes of σ_{xx} along the y axis, (b) Stress changes of σ_{yy} along the y axis, (c) Stress changes of σ_{zz} along the y axis, (d) Stress changes of σ_{xy} along $x = -1000$ m, (e) Stress changes of σ_{xz} along the x axis, and (f) Stress changes of σ_{yz} along the y axis.

high temperatures. Common phyllosilicate minerals, including smectite, illite, muscovite, chlorite and talc, tend to return low frictional strength and promote the aseismic creep behavior due to minimized gouge particle interlocking and dilation resulting from their sheet structures (Morgan and Boettcher, 1999; Kohli and Zoback, 2013). Carbonate minerals (primarily calcite and dolomite) exhibit comparable frictional strength to the tectosilicates but the complex frictional stability behaviors depend on temperature, effective stress and fluid chemical environment (Verberne et al., 2013, 2015). In this study, we conduct the fault reactivation experiments on only several representative rock gouges (granite, sandstone and slate) recovered from the outcrops - these gouges may not fully reflect the fault stability of the whole basement in southeastern Sichuan Basin, but the results apparently show the trend that clay-lean faults are prone to promote seismic sliding with the

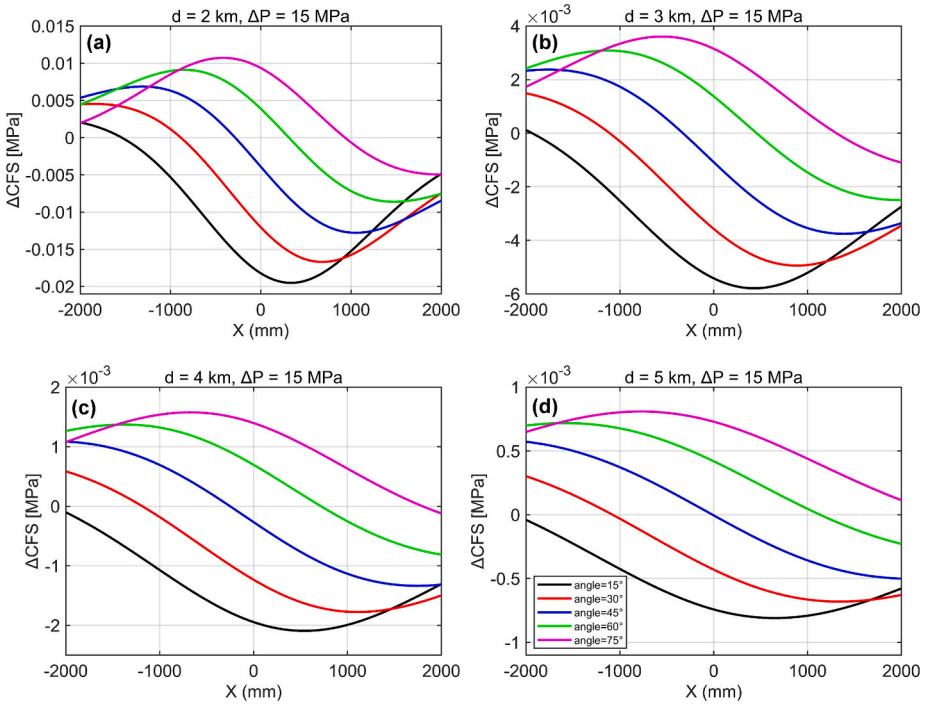

Fig. 13. Changes in Coulomb failure stress (ΔCFS) along the x axis due to three prismatic injection zones at $\Delta P = 15$ MPa and different distances, (a) $d = 2$ km, (b) $d = 3$ km, (c) $d = 4$ km, and (d) $d = 5$ km.

clay-rich bearing faults the converse.

From its tectonic structure (Fig. 1a), the Sichuan Basin remains seismically active with this basin exposed to the complex tectonic stresses resulting from the tectonics of the western Tibet Plateau, the northern Qinling-Dabie Orogenic Belt, and the eastern Jiangnan-Xuefeng Orogenic Belt (Xu et al., 2019; Liu et al., 2021). Faults in granitoid or sandstone basement are potentially unstable (from the experiments) and the basement in the Sichuan Basin is also tectonically active, indicating the possibility of nucleating natural destructive earthquakes (Li et al., 2010; Su et al., 2023). The experimental results, combined with the tectonic environments, also identify the existence of potentially seismogenic zones in the basement of the southeastern Sichuan basin, with the gouge mineral composition as one of the most important intrinsic factors to determine basement gouge bearing fault stability (Ikari et al., 2011; Fang et al., 2018; An et al., 2024). Although the testing temperatures and pressures in this study correspond only to a depth of 8 km, the observed velocity-weakening and stick-slip behaviors in sandy or granitoid gouge are also applicable for a shallower depth of ~6 km ($T \approx 190$ °C) as the velocity-weakening behavior in granitoid gouges is observed at temperatures lower than ~100 °C (Blanpied et al., 1991; Kolawole et al., 2019). Hence, the basement rocks in the southeastern Sichuan Basin are potentially active seismogenic zones. This is an important prerequisite for seismic reactivation of basement faults in shallower geo-energy extraction and storage.

We then analyze the mechanisms of basement fault reactivation due to geo-energy extraction and storage with the analysis based on the third models in Fig. S1. It is not likely that the first model alone is a potential mechanism to trigger basement fault instability as the current fluid injection zones are several kilometers (>2 km) away from the basement. As suggested by many relevant studies (Rubinstein and Mahani, 2015; Guglielmi et al., 2015; Fan et al., 2019), pore fluid diffusion generally extend to hundreds of meters from injection and thus the direct pore pressure communication could be an important mechanism for adjacent fault reactivation. This is evident in our previous study (An et al., 2020b) where ten stages of hydraulic fracturing could directly reactivate a pre-existing fault located at the toe of a horizontal well (N201 in the Changning block of the southeastern Sichuan Basin).

The second model highlights the role of stress transfer from industrial activities in shallow reservoirs (Deng et al., 2016; Goebel et al., 2017). From the induced ΔCFS values at different distances (Fig. 13), fluid injection produces comparable ΔCFS values with magnitudes higher than 10^{-2} MPa within a distance of 2 km, enabling the triggering of critically-stressed faults. The ΔCFS values calculated from the multiage stage hydraulic fracturing in a well pad in the Changning block also support this conclusion. Two kilometers could be the shortest distance from the pressurized zone to the basement in the southeastern Sichuan basin. However, it should be noted that the above calculations are only applicable for a single injection site and dozens of injection sites may be operated simultaneously in one block. The induced ΔCFS values could be much higher than the current values, thus enabling earthquake triggering at a greater distance, i.e., within the basement zones. Meanwhile, poroelastic triggering of seismicity is also demonstrated in the seismic data (An et al., 2024). The dense seismic array deployed in the Changning block recorded the background seismicity ($M_L \geq 0$) from 28th February 2019 to 6th May 2019 - for ~70 days. The seismic data apparently indicate three peaks in earthquake occurrence with depth. The first peak corresponds to the hydraulic fracturing zone with the other two peaks located at depths of ~1.5 and ~2.5 km below the fracturing zone. It is likely that these remote earthquakes occur due to the poroelastic stress transfer from slip on shallow faults. These remote seismic events suggest the possibility of poroelastic stress triggered earthquakes. The potential for an active seismogenic zone, is evident from the fault shear experiments and simulations.

Apart from the two widely-accepted mechanisms, the third model also provides a potential mechanism for earthquake triggering in the southeastern Sichuan Basin based on the seismic reflection profile of Fig. 14. There are many large thrust faults extending from the current fluid injection zones (such as in the Lower Silurian Longmaxi formation) to the basement in the Changning and Zhaotong blocks. Base on our previous study that explore the stability of Longmaxi shale gouges (An et al., 2020a), almost 95 % of the shale gouges show aseismic sliding and creep under in-situ hydrothermal conditions. This shows that aseismic fault sliding around the fluid injection zone could possibly load the remote fault reactivation in the basement. This extrapolation is based on

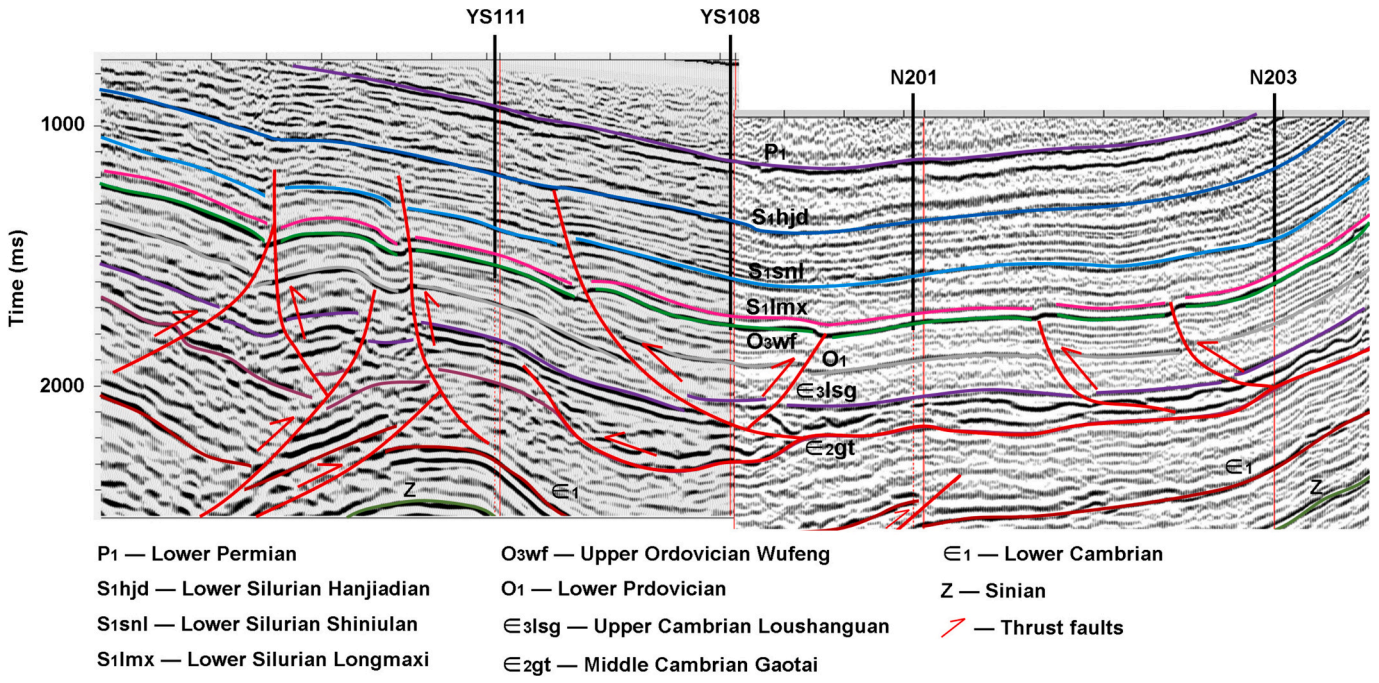

Fig. 14. Seismic reflection profile showing the geologic structures and tectonic settings of the Changning-Zhaotong blocks by four exploration wells (N203, N201, YS108 and YS 111). The Longmaxi formation is currently an important formation for shale gas extraction and potential carbon dioxide sequestration in the southeastern Sichuan basin. The locations of these wells are noted in An et al. (2021).

the simulation results of Eyre et al. (2019) where distant fault ruptures could be induced by aseismic fault slip at reservoir depth. Meanwhile, the large thrust faults below the reservoir also act as fluid channels for injected fluids to deeper depths but whether the fluid could flow kilometers away needs further verification (Eyre et al., 2019; Kolawole et al., 2019; Atkinson et al., 2020; Moein et al., 2023). A combination of the above explanations could explain the potential for fault reactivation in southeastern Sichuan Basin. Our fault reactivation experiments indicate that the basement is potentially seismogenic and our simulation results confirm that poroelastic stress could reactivate remote and critically-stressed basement faults. The seismic reflection profile provides important supplementary information and indicates the presence of dense arrays of large thrust faults existing within the reservoir zone and basement. This further provides the possibility for remote earthquake triggering by aseismic fault loading and the long-distance fluid diffusions.

4.2. *Implications for understanding injection-induced seismicity*

Our experimental and modelling results have important implications for understanding injection-induced seismicity distant from the fluid injection zones, such as seismicity within basement rocks. As depicted in Fig. 15, the basement fault instability is influenced by aseismic slip within the pressurized zone, poroelastic stress transfer from fluid injection or hydraulic fracturing and the composition of fault gouge minerals. Hence, injection-induced seismicity typically results from a combination of different influencing factors rather than a single factor. Geologic structure, tectonic setting and anthropogenic activities all affect the occurrence of induced seismicity in the basement. In addition, understanding the basement fault stability is also vital for the safety of local residents and buildings as the hydrothermal environment of the basement promotes the nucleation of destructive earthquakes, especially in the seismically active southeastern Sichuan basin. Our current research provides guidance in understanding the relationship between geo-engineering activities and basement earthquakes and further reducing the seismic hazards.

We also compare the induced seismicity in Sichuan Basin basement

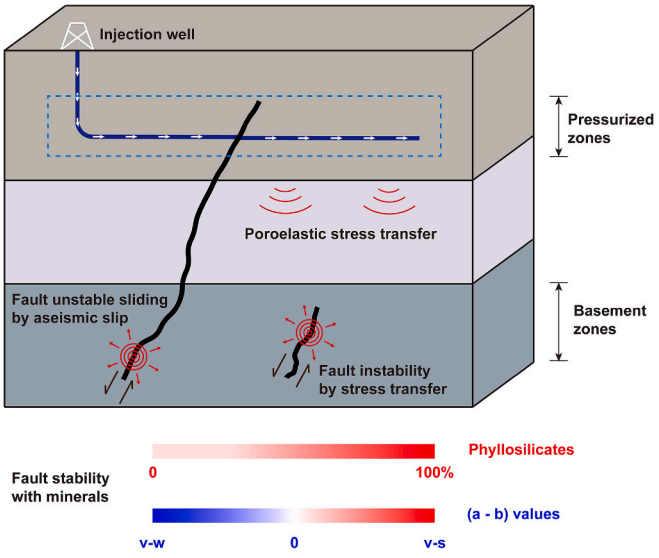

Fig. 15. Schematic showing mechanisms of basement fault instability induced by fluid injection. Basement fault stability could be affected by aseismic fault slip, poroelastic stress transfer and fault gouge mineral compositions.

with that in Oklahoma in the United States. The seismicity rate in the eastern and central US has increased nearly fortyfold compared to the last century. This is primarily due to the large-volume wastewater injection into the deep sedimentary layers, with Oklahoma experiencing the highest earthquake rate increase in the US (Ellsworth, 2013; Keranen et al., 2014; Rubinstein and Mahani, 2015). Moreover, the 2011 M 5.7 Prague and 2016 M 5.8 Pawnee earthquakes in Oklahoma have been regarded as the two largest induced earthquakes related to wastewater disposal in Oklahoma (Yeck et al., 2017; Skoumal et al., 2018). Mechanisms of clusters of earthquakes in Oklahoma also include direct pore pressure increases within the fault zones and poroelastic stress transfer from the injection zone to remote faults. These show that our two models

represent pervasive mechanisms to interpret the adjacent and remote injection-induced seismicity. Meanwhile, Kolawole et al. (2019) reveal that the Oklahoma basement also shows a high potential for seismic reactivation for two primary reasons. Firstly, basement-rooted faults penetrate into the upper sedimentary layers and thus provide the pathways for injected fluid migration. Secondly, the basement faults are seismically unstable at the hypocenter depth. The seismic reactivation potential in Oklahoma basement is similar to that of the southeastern Sichuan Basin. These two cases both indicate the importance of linking the basement geological structures with fluid injection activities in interpreting induced earthquakes.

5. Conclusions

We report a systematic study that explores the effect of geo-energy extraction and storage activities on the stability of basement faults in the southeastern Sichuan basin. We recovered outcrop samples of basement rocks to generate the simulated fault gouge and conduct the fault friction experiments under hydrothermal conditions to assess the stability of rock gouges. We then calculate the induced poroelastic stresses and Coulomb failure stresses from various fluid injection scenarios to define the poroelastic effects on basement fault stability. Finally, the experimental-modelling results combined with the seismic reflection profile are employed to analyze the seismic potential of basement faults. The main conclusions are as follows:

Basement rock characteristics. The basement rocks in the southeastern Sichuan basin primarily include clay-lean granites and sandstones and clay-rich slates, with clay contents ranging from 4 to 70 *wt*%. The muscovite and clinochlore are two dominant clay minerals.

Experimental results. Clay content is the dominant factor that controls the gouge frictional strength and stability under hydrothermal conditions. The frictional strengths of the selected rock gouges are primarily within 0.5–0.7. With an increase in clay contents, the gouge frictional strengths monotonically decrease and a transition from velocity-weakening to velocity-strengthening behavior is observed. Granitoid and sandy layers at the basement could represent principal seismogenic zones.

Modelling results. A single fluid injection site incorporating three prismatic zones induces ΔCFS values higher than 10^{-2} MPa within a distance of 2 km and reactivates critically-stresses faults, with ΔCFS values decaying rapidly at longer distances.

Seismic reflection results. The seismic reflection profile shows large thrust faults extending from the fluid injection zones to the basement, which indicates the potential for unstable sliding of basement faults promoted by the reservoir fault aseismic slips.

Implications. Our results indicate that basement fault stability affected by fluid injection can be understood from a combination of influencing factors rather than a single factor, including fault aseismic slip within pressurized zones, poroelastic stress transfer from fluid injection or hydraulic fracturing and the mineral compositions of fault gouges. Understanding these results aids in reducing the seismic hazard during geo-energy extraction and storage in the southeastern Sichuan basin and similar sites.

CRediT authorship contribution statement

Mengke An: Writing – original draft, Funding acquisition, Formal analysis, Data curation, Conceptualization. **Rui Huang:** Writing – review & editing, Validation, Formal analysis. **Derek Elsworth:** Writing – review & editing, Validation, Data curation. **Fengshou Zhang:** Writing – review & editing. **Zhen-Yu Yin:** Writing – review & editing. **Liuke Huang:** Writing – review & editing. **Zhengyu Xu:** Writing – review & editing, Methodology.

Declaration of competing interest

No.

Acknowledgements

This research is funded by the National Natural Science Foundation of China (42107163, 42320104003). DE acknowledges the support from the G. Albert Shoemaker endowment. We appreciate the assistances from Changrong He, Jianye Chen and Wenming Yao in conducting the friction experiments and Egor Dontsov in performing the stress perturbation calculations.

Appendix A. Supplementary data

Supplementary data to this article can be found online at https://doi.org/10.1016/j.tecto.2025.230628.

Data availability

Data will be made available on request.

References

An, M., Zhang, F., Elsworth, D., Xu, Z., Chen, Z., Zhang, L., 2020a. Friction of Longmaxi shale gouges and implications for seismicity during hydraulic fracturing. J. Geophys. Res. Solid Earth 125, e2020JB019885. https://doi.org/10.1029/2020JB019885.

An, M., Zhang, F., Chen, Z., Elsworth, D., Zhang, L., 2020b. Temperature and fluid pressurization effects on frictional stability of shale faults reactivated by hydraulic fracturing in the Changning block, Southwest China. J. Geophys. Res. Solid Earth 125, e2020JB019584. https://doi.org/10.1029/2020JB019584.

An, M., Zhang, F., Dontsov, E., Elsworth, D., Zhu, H., Zhao, L., 2021. Stress perturbation caused by multistage hydraulic fracturing: Implications for deep fault reactivation. Int. J. Rock Mech. Min. Sci. 141, 104704. https://doi.org/10.1016/j.ijrmms.2021.104704.

An, M., Elsworth, D., Zhang, F., Huang, R., Li, J., Xu, Z., Zhong, Z., He, M., 2024. Brittle sedimentary strata focus a multimodal depth distribution of seismicity during hydraulic fracturing in the Sichuan Basin, Southwest China. Tectonophysics 880, 230332. https://doi.org/10.1016/j.tecto.2024.230332.

Atkinson, G.M., Eaton, D.W., Igonin, N., 2020. Developments in understanding seismicity triggered by hydraulic fracturing. Nat. Rev. Earth Environ. 1, 264–277. https://doi.org/10.1038/s43017-020-0049-7.

Azad, M., Garagash, D.I., Satish, M., 2017. Nucleation of dynamic slip on a hydraulically fractured fault. J. Geophys. Res. Solid Earth 122 (4), 2812–2830. https://doi.org/10.1002/2016JB013835.

Bao, X., Eaton, D.W., 2016. Fault activation by hydraulic fracturing in western Canada. Science 354 (6318), 1406–1409. https://doi.org/10.1126/science.aag2583.

Belzer, B.D., French, M.E., 2022. Frictional constitutive behavior of chlorite at low shearing rates and hydrothermal conditions. Tectonophysics 837, 229435. https://doi.org/10.1016/j.tecto.2022.229435.

Bhattacharya, P., Viesca, R.C., 2019. Fluid-induced aseismic fault slip outpaces pore-fluid migration. Science 364 (6439), 464–468. https://doi.org/10.1126/science.aaw7354.

Bickle, M.J., 2009. Geological carbon storage. Nat. Geosci. 2, 815–818. https://doi.org/10.1038/ngeo687.

Blanpied, M.L., Lockner, D.A., Byerlee, J.D., 1991. Fault stability inferred from granite sliding experiments at hydrothermal conditions. Geophys. Res. Lett. 18 (4), 609–612. https://doi.org/10.1029/91GL00469.

Brace, W.F., Byerlee, J.D., 1966. Stick-slip as a mechanism for earthquakes. Science 153 (3739), 990–992. https://doi.org/10.1126/science.153.3739.990.

Caine, J.S., Evans, J.P., Forster, C.B., 1996. Fault zone architecture and permeability structure. Geology 24 (11), 1025–1028, 10.1130/0091-7613(1996)024<1025:FZAAPS>2.3.CO;2.

Chang, K.W., Segall, P., 2016a. Injection-induced seismicity on basement faults including poroelastic stressing. J. Geophys. Res. Solid Earth 121, 2708–2726. https://doi.org/10.1002/2015JB012561.

Chang, K.W., Segall, P., 2016b. Seismicity on basement faults induced by simultaneous fluid injection—Extraction. Pure Appl. Geophys. 173 (8), 2621–2636. https://doi.org/10.1007/s00024-016-1319-7.

Chen, H., Meng, X., Niu, F., Tang, Y., Yin, C., Wu, F., 2018. Microseismic monitoring of stimulating shale gas reservoir in SW China: 2. Spatial clustering controlled by the preexisting faults and fractures. J. Geophys. Res. Solid Earth 123 (2), 1659–1672. https://doi.org/10.1002/2017JB014491.

Chen, Z., Shi, L., Xiang, D., 2017. Mechanism of casing deformation in the Changning-Weiyuan national shale gas demonstration area and countermeasures. Natl. Gas Industry B 4 (1), 1–6. https://doi.org/10.1016/j.ngib.2017.07.001.

Deng, K., Liu, Y., Harrington, R.M., 2016. Poroelastic stress triggering of the December 2013 Crooked Lake, Alberta, induced seismicity sequence. Geophys. Res. Lett. 43 (16), 8482–8491. https://doi.org/10.1002/2016GL070421.

Dieterich, J.H., 1979. Modeling of rock friction: 1. Experimental results and constitutive equations. J. Geophys. Res. 84 (B5), 2161. https://doi.org/10.1029/JB084iB05p02161.
Ellsworth, W.L., 2013. Injection-induced earthquakes. Science 341 (6142). https://doi.org/10.1126/science.1225942.
Elsworth, D., Spiers, C.J., Niemeijer, A.R., 2016. Understanding induced seismicity. Science 354 (6318), 1380–1381. https://doi.org/10.1126/science.aal2584.
Eyre, T.S., Eaton, D.W., Garagash, D.I., Zecevic, M., Venieri, M., Weir, R., Lawton, D.C., 2019. The role of aseismic slip in hydraulic fracturing-induced seismicity. Sci. Adv. 5, eaav7172. https://doi.org/10.1126/sciadv.aav7172.
Fagereng, Å., Ikari, M.J., 2020. Low-temperature frictional characteristics of chlorite-epidote-amphibole assemblages: Implications for strength and seismic style of retrograde fault zones. J. Geophys. Res. Solid Earth 125 (4), e2020JB019487. https://doi.org/10.1029/2020JB019487.
Fan, Z., Eichhubl, P., Newell, P., 2019. Basement fault reactivation by fluid injection into sedimentary reservoirs: Poroelastic effects. J. Geophys. Res. Solid Earth 124, 7354–7369. https://doi.org/10.1029/2018JB017062.
Fang, Y., Elswrth, D., Wang, C., Jia, Y., 2018. Mineralogical controls on frictional strength, stability, and shear permeability evolution of fractures. J. Geophys. Res. Solid Earth 123 (5), 3549–3563. https://doi.org/10.1029/2017JB015338.
Garagash, D.I., Germanovich, L.N., 2012. Nucleation and arrest of dynamic slip on a pressurized fault. J. Geophys. Res. Solid Earth 117 (B10). https://doi.org/10.1029/2012JB009209.
Ge, S., Saar, M.O., 2022. Review: Induced seismicity during geoenergy development—a hydromechanical perspective. J. Geophys. Res. Solid Earth 127 (3), e2021JB023141. https://doi.org/10.1029/2021JB023141.
Goebel, T.H.W., Weingarten, M., Chen, X., Haffener, J., Brodsky, E.E., 2017. The 2016 M_w 5.1 Fairview, Oklahoma earthquakes: evidence for long-range poroelastic triggering at >40 km from fluid disposal wells. Earth Planet. Sci. Lett. 472, 50–61. https://doi.org/10.1016/j.epsl.2017.05.011.
Gu, J.-C., Rice, J.R., Ruina, A.L., Tse, S.T., 1984. Slip motion and stability of a single degree of freedom elastic system with rate and state dependent friction. J. Mech. Phys. Solids 32 (3), 167–196. https://doi.org/10.1016/0022-5096(84)90007-3.
Guglielmi, Y., Cappa, F., Avouac, J.-P., Henry, P., Elsworth, D., 2015. Seismicity triggered by fluid injection-induced aseismic slip. Science 348, 1224–1226. https://doi.org/10.1126/science.aab0476.
Harris, R.A., 1998. Introduction to special section: stress triggers, stress shadows, and implications for seismic hazard. J. Geophys. Res. Solid Earth 103 (B10), 24347–24358. https://doi.org/10.1029/98jb01576.
He, C., Yao, W., Wang, Z., Zhou, Y., 2006. Strength and stability of frictional sliding of gabbro gouge at elevated temperatures. Tectonophysics 427 (1–4), 217–229. https://doi.org/10.1016/j.tecto.2006.05.023.
He, C., Luo, L., Hao, Q., Zhou, Y., 2013. Velocity-weakening behavior of plagioclase and pyroxene gouges and stabilizing effect of small amounts of quartz under hydrothermal conditions. J. Geophys. Res. Solid Earth 118 (7), 3408–3430. https://doi.org/10.1002/jgrb.50280.
He, D., Lu, R., Huang, H., Wang, X., Jiang, X., Zhang, W., 2019. Tectonic and geological setting of the earthquake hazards in the Changning shale gas development zone, Sichuan Basin, SW China. Petrol. Explorat. Develop. 46 (5), 1051–1064. https://doi.org/10.1016/S1876-3804(19)60262-4.
Ikari, M.J., Marone, C., Saffer, D.M., 2011. On the relation between fault strength and frictional stability. Geology 39 (1), 83–86. https://doi.org/10.1130/G31416.1.
Keranen, K.M., Weingarten, M., Abers, G.A., Bekins, B.A., Ge, S., 2014. Sharp increase in Central Oklahoma seismicity since 2008 induced by massive wastewater injection. Science 345 (6195), 448–451. https://doi.org/10.1126/science.1255802.
Kettlety, T., Verdon, J.P., Werner, M.J., Kendall, J.M., Budge, J., 2019. Investigating the role of elastostatic stress transfer during hydraulic fracturing-induced fault activation. Geophys. J. Int. 217 (2), 1200–1216. https://doi.org/10.1093/gji/ggz080.
Kohli, A.H., Zoback, M.D., 2013. Frictional properties of shale reservoir rocks. J. Geophys. Res. Solid Earth 118, 5109–5125. https://doi.org/10.1002/jgrb.50346.
Kolawole, F., Johnston, C.S., Morgan, C.B., Chang, J.C., Marfurt, K.J., Lockner, D.A., Reches, Z., Carpenter, B.M., 2019. The susceptibility of Oklahoma's basement to seismic reactivation. Nat. Geosci. 12, 839–844. https://doi.org/10.1038/s41561-019-0440-5.
Lei, X., Huang, D., Su, J., Jiang, G., Wang, X., Wang, H., et al., 2017. Fault reactivation and earthquakes with magnitudes of up to M_w 4.7 induced by shale-gas hydraulic fracturing in Sichuan Basin, China. Sci. Rep. 7, 7971. https://doi.org/10.1038/s41598-017-08557-y.
Lei, X., Wang, Z., Su, J., 2019. Possible link between long-term and short-term water injections and earthquakes in salt mine and shale gas site in Changning, South Sichuan Basin, China. Earth Planet. Phys. 3 (6), 510–525. https://doi.org/10.26464/epp2019052.
Li, J., Xu, J., Zhang, H., Yang, W., Tan, Y., Zhang, F., Meng, L., Zang, Y., Miao, S., Guo, C., Li, Z., Lu, R., Sun, J., 2023. High seismic velocity structures control moderate to strong induced earthquake behaviors by shale gas development. Commun. Earth Environ. 4, 188. https://doi.org/10.1038/s43247-023-00854-x.
Li, Y., Jia, D., Shaw, J.H., Hubbard, J., Lin, A., Wang, M., Luo, L., Li, H., Wu, L., 2010. Structural interpretation of the coseismic faults of the Wenchuan earthquake: Three-dimensional modeling of the Longmen Shan fold-and-thrust belt. J. Geophys. Res. Solid Earth 115 (B4). https://doi.org/10.1029/2009JB006824.
Liu, J., Zahradník, J., 2020. The 2019 M_W 5.7 Changning earthquake, Sichuan Basin, China: a shallow doublet with different faulting styles. Geophys. Res. Lett. 47 (4), e2019GL085408. https://doi.org/10.1029/2019GL085408.
Liu, S., Yang, Y., Deng, B., Zhong, Y., Wen, L., Sun, W., Li, Z., Jansa, L., Li, J., Song, J., Zhang, X., Peng, H., 2021. Tectonic evolution of the Sichuan Basin, Southwest China. Earth-Sci. Rev. 213, 103470. https://doi.org/10.1016/j.earscirev.2020.103470.
Liu, Y., He, C., 2020. Friction properties of hornblende and implications for slow-slip events in subduction zones. Tectonophysics 796, 228644. https://doi.org/10.1016/j.tecto.2020.228644.
Ma, X., Xie, J., 2018. The progress and prospects of shale gas exploration and development in southern Sichuan Basin, SW China. Petrol. Explorat. Develop. 45 (1), 172–182. https://doi.org/10.1016/S1876-3804(18)30018-1.
Marone, C., 1998. Laboratory-derived friction laws and their application to seismic faulting. Annu. Rev. Earth Planet. Sci. 26 (1), 643–696. https://doi.org/10.1146/annurev.earth.26.1.643.
Meng, L., McGarr, A., Zhou, L., Zang, Y., 2019. An investigation of seismicity induced by hydraulic fracturing in the Sichuan Basin of China based on data from a temporary seismic network. Bull. Seismol. Soc. Am. 109 (1), 348–357. https://doi.org/10.1785/0120180310.
Moein, M.J.A., Langenbruch, C., Schultz, R., Grigoli, F., Ellsworth, W.L., Wang, R., Rinaldi, A.P., Shapiro, S., 2023. The physical mechanisms of induced earthquakes. Nat. Rev. Earth Environ. 4, 847–863. https://doi.org/10.1038/s43017-023-00497-8.
Morgan, J.K., Boettcher, M.S., 1999. Numerical simulations of granular shear zones using the distinct element method: 1. Shear zone kinematics and the micromechanics of localization. J. Geophys. Res. 104 (B2), 2703–2719. https://doi.org/10.1029/1998JB900056.
Okada, Y., 1992. Internal deformation due to shear and tensile faults in a half-space. Bull. Seismol. Soc. Am. 82 (2), 1018–1040.
Okamoto, A.S., Verberne, B.A., Niemeijer, A.R., Takahashi, M., Shimizu, I., Ueda, T., Spiers, C.J., 2019. Frictional properties of simulated chlorite gouge at hydrothermal conditions: Implications for subduction megathrusts. J. Geophys. Res. Solid Earth 124 (5), 4545–4565. https://doi.org/10.1029/2018JB017205.
Okamoto, A.S., Niemeijer, A.R., Takeshita, T., Verberne, B.A., Spiers, C.J., 2020. Frictional properties of actinolite-chlorite gouge at hydrothermal conditions. Tectonophysics 779, 228377. https://doi.org/10.1016/j.tecto.2020.228377.
Raleigh, C.B., Healy, J.H., Bredehoeft, J.D., 1976. An experiment in earthquake control at Rangely, Colorado. Science 191 (4233), 1230–1237. https://doi.org/10.1126/science.191.4233.1230.
Rubinstein, J.L., Mahani, A.B., 2015. Myths and facts on wastewater injection, hydraulic fracturing, enhanced oil recovery, and induced seismicity. Seismol. Res. Lett. 86 (4), 1060–1067. https://doi.org/10.1785/0220150067.
Ruina, A., 1983. Slip instability and state variable friction laws. J. Geophys. Res. Solid Earth 88 (B12), 10359–10370. https://doi.org/10.1029/JB088iB12p10359.
Segall, P., Lu, S., 2015. Injection-induced seismicity: Poroelastic and earthquake nucleation effects. J. Geophys. Res. Solid Earth 120 (7), 5082–5103. https://doi.org/10.1002/2015JB012060.
Skoumal, R.J., Ries, R., Brudzinski, M.R., Barbour, A.J., Currie, B.S., 2018. Earthquakes induced by hydraulic fracturing are pervasive in Oklahoma. J. Geophys. Res. Solid Earth 123, 10918–10935. https://doi.org/10.1029/2018JB016790.
Stein, R.S., 1999. The role of stress transfer in earthquake occurrence. Nature 402 (6762), 605–609. https://doi.org/10.1038/45144.
Su, Z., Bürgmann, R., Wang, E., 2023. The origin of seismic and tectonic activity underlying the Sichuan Basin, Central China. Tectonics 42 (5), e2022TC007629. https://doi.org/10.1029/2022TC007629.
Sumy, D.F., Cochran, E.S., Keranen, K.M., Wei, M., Abers, G.A., 2014. Observations of static Coulomb stress triggering of the November 2011 M5.7 Oklahoma earthquake sequence. J. Geophys. Res. Solid Earth 119 (3), 1904–1923. https://doi.org/10.1002/2013JB010612.
Sun, X., Yang, P., Zhang, Z., 2017. A study of earthquakes induced by water injection in the Changning salt mine area, SW China. J. Asian Earth Sci. 136, 102–109. https://doi.org/10.1016/j.jseaes.2017.01.030.
Sun, X., Alcalde, J., Gomez-Rivas, E., Struth, L., Johnson, G., Travé, A., 2020. Appraisal of CO_2 storage potential in compressional hydrocarbon-bearing basins: Global assessment and case study in the Sichuan Basin (China). Geosci. Front. 11 (6), 2309–2321. https://doi.org/10.1016/j.gsf.2020.02.008.
Tan, Y., Qian, J., Hu, J., Zhang, H., Xing, H., Li, J., Xu, J., Yang, W., Gu, N., Miao, S., 2023. Tomographic evidences for hydraulic fracturing induced seismicity in the Changning shale gas field, southern Sichuan Basin, China. Earth Planet. Sci. Lett. 605, 118021. https://doi.org/10.1016/j.epsl.2023.118021.
Tembe, S., Lockner, D.A., Wong, T.-F., 2010. Effect of clay content and mineralogy on frictional sliding behavior of simulated gouges: Binary and ternary mixtures of quartz, illite, and montmorillonite. J. Geophys. Res. 115, B03416. https://doi.org/10.1029/2009JB006383.
Verberne, B.A., Spiers, C.J., Niemeijer, A.R., De Bresser, J.H.P., De Winter, D.A.M., Plümper, O., 2013. Frictional properties and microstructure of calcite-rich fault gouges sheared at sub-seismic sliding velocities. Pure Appl. Geophys. 171 (10), 2617–2640. https://doi.org/10.1007/s00024-013-0760-0.
Verberne, B.A., Niemeijer, A.R., De Bresser, J.H.P., Spiers, C.J., 2015. Mechanical behavior and microstructure of simulated calcite fault gouge sheared at 20-600 °C: Implications for natural faults in limestones. J. Geophys. Res. Solid Earth 120, 8169–8196. https://doi.org/10.1002/2015JB012292.
Xi, Y., Li, J., Liu, G., Cha, C., Fu, Y., 2018. Numerical investigation for different casing deformation reasons in Weiyuan-Changning shale gas field during multistage hydraulic fracturing. J. Petrol. Sci. Eng. 163, 691–702. https://doi.org/10.1016/j.petrol.2017.11.020.
Xu, Z., Jiang, S., Yao, G., Liang, X., Xiong, S., 2019. Tectonic and depositional setting of the lower Cambrian and lower Silurian marine shales in the Yangtze Platform, South China: Implications for shale gas exploration and production. J. Asian Earth Sci. 170, 1–19. https://doi.org/10.1016/j.jseaes.2018.10.023.

Yang, W., Chen, G., Meng, L., Zang, Y., Zhang, H., Li, J., 2021. Determination of the local magnitudes of small earthquakes using a dense seismic array in the Changning-Zhaotong Shale Gas Field, Southern Sichuan Basin. Earth Planet. Phys. 5 (6), 532–546. https://doi.org/10.26464/epp2021026.

Yeck, W.L., Hayes, G.P., McNamara, D.E., Rubinstein, J.L., Barnhart, W.D., Earle, P.S., Benz, H.M., 2017. Oklahoma experiences largest earthquake during ongoing regional wastewater injection hazard mitigation efforts. Geophys. Res. Lett. 44, 711–717. https://doi.org/10.1002/2016GL071685.

Zhang, F., Yin, Z., Chen, Z., Maxwell, S., Zhang, L., Wu, Y., 2019a. Fault reactivation and induced seismicity during multistage hydraulic fracturing: microseismic analysis and geomechanical modeling. SPE J. 25 (2). https://doi.org/10.2118/199883-PA.

Zhang, F., An, M., Zhang, L., Fang, Y., Elsworth, D., 2019b. The role of mineral composition on the frictional and stability properties of powdered reservoir rocks. J. Geophys. Res. Solid Earth 124, 1480–1497. https://doi.org/10.1029/2018JB016174.

Zhang, L., He, C., 2013. Frictional properties of natural gouges from Longmenshan fault zone ruptured during the Wenchuan M_w 7.9 earthquake. Tectonophysics 594, 149–164. https://doi.org/10.1016/j.tecto.2013.03.030.

Zhang, L., He, X., Li, X., Li, K., He, J., Zhang, Z., et al., 2022. Shale gas exploration and development in the Sichuan Basin: Progress, challenge and countermeasures. Natl. Gas Industry B 9 (2), 176–186. https://doi.org/10.1016/j.ngib.2021.08.024.

Zoback, M.D., 2007. Reservoir Geomechanics. Cambridge University Press, New York.